SERDP

WHITE PAPER

# Inversion in Transient Electromagnetic Induction Sensing of Underwater Metallic Munitions with Sensor Positioning Errors

Stephen Billings
Lin-Ping Song
***Black Tusk Geophysics***

**July 2023**

**SERDP Project MR19-1261**

**DISTRIBUTION STATEMENT A**
This document has been cleared for public release.

# REPORT DOCUMENTATION PAGE

*Form Approved*
*OMB No. 0704-0188*

**1. REPORT DATE** *(DD-MM-YYYY)*
31/07/2023

**2. REPORT TYPE**
SERDP White Paper

**3. DATES COVERED** *(From - To)*
9/23/2019 - 9/23/2024

**4. TITLE AND SUBTITLE**
Inversion in Transient Electromagnetic Induction Sensing of Underwater Metallic Munitions with Sensor Positioning Errors

**5a. CONTRACT NUMBER**
19-C-0023

**5b. GRANT NUMBER**

**5c. PROGRAM ELEMENT NUMBER**

**6. AUTHOR(S)**
Stephen Billings
Lin-Ping Song
Black Tusk Geophysics

**5d. PROJECT NUMBER**
MR19-1261

**5e. TASK NUMBER**

**5f. WORK UNIT NUMBER**

**7. PERFORMING ORGANIZATION NAME(S) AND ADDRESS(ES)**
Black Tusk Geophysics
401 / 1755 West Broadway
Vancouver, BC V6J4S5

**8. PERFORMING ORGANIZATION REPORT NUMBER**
MR19-1261

**9. SPONSORING/MONITORING AGENCY NAME(S) AND ADDRESS(ES)**
Strategic Environmental Research and Development Program (SERDP)
4800 Mark Center Drive, Suite 16F16
Alexandria, VA 22350-3605

**10. SPONSOR/MONITOR'S ACRONYM(S)**
SERDP

**11. SPONSOR/MONITOR'S REPORT NUMBER(S)**
MR19-1261

**12. DISTRIBUTION/AVAILABILITY STATEMENT**
DISTRIBUTION STATEMENT A. Approved for public release: distribution unlimited.

**13. SUPPLEMENTARY NOTES**

**14. ABSTRACT**
Contamination with underwater munitions has been a long-standing issue in marine environments. There have been various efforts to develop sensing techniques that can be used to help remediate shallow water sites contaminated by munitions. Over the years, marine electromagnetic induction (EMI) sensing has emerged as a promising technique for underwater munitions detection and characterization. Marine EMI sensing, which is adopted from the terrestrial case, aims to identify and classify potential UXO items based on the polarizabilities (the physical property) of a target extracted from measurements.

**15. SUBJECT TERMS**
Transient Electromagnetic Induction Sensing, Underwater Metallic Munitions, Sensor Positioning Errors, Advanced Marine EMI Processing Techniques, Munitions Detection and Classification

**16. SECURITY CLASSIFICATION OF:**

| a. REPORT | b. ABSTRACT | c. THIS PAGE | 17. LIMITATION OF ABSTRACT | 18. NUMBER OF PAGES |
|---|---|---|---|---|
| UNCLASS | UNCLASS | UNCLASS | UNCLASS | 33 |

**19a. NAME OF RESPONSIBLE PERSON**
Stephen Billings

**19b. TELEPHONE NUMBER** *(Include area code)*
720-306-1165

# WHITE PAPER

Project: MR19-1261

## TABLE OF CONTENTS

## LIST OF FIGURES

# ACRONYMS

| | |
|---|---|
| 1D | One-dimensional |
| DoD | Department of Defense |
| EMI | Electromagnetic Induction |
| IMLI | Independent Model Location Inversion |
| ISO | Industry Standard Object |
| JETSP | Joint Estimation of Target and Survey/sensing Parameters |
| m | meter |
| ms | millisecond |
| Rx | Receiver |
| s | second |
| TEM | Transient Electromagnetic Induction |
| TOI | Target of Interest |
| Tx | Transmitter |
| UltraTEM | Ultra Transient ElectroMagentic Induction |
| UltraTEMA | UltraTEM Array |
| UXO | Unexploded Ordnance |

# 1. Introduction

Contamination with underwater munitions has been a long-standing issue in marine environments. There have been various efforts to develop sensing techniques that can be used to help remediate shallow water sites contaminated by munitions. Over the years, marine electromagnetic induction (EMI) sensing has emerged as a promising technique for underwater munitions detection and characterization. Marine EMI sensing, which is adopted from the terrestrial case, aims to identify and classify potential UXO items based on the polarizabilities (the physical property) of a target extracted from measurements.

Marine EMI sensing faces with some unique physical and operational challenges, including reduced signal levels due to stand-off distance to seafloor, the obscuring of target signals by the conductive background response of sea-water, reduced positional accuracy and non-uniform data coverage due to navigational difficulties. In this paper, we focus on addressing the challenge of sensor positional uncertainty. In the marine environment, accurate positioning of an EMI survey is more difficult than for the terrestrial case. Relative positional errors between adjacent survey lines can lead to an erroneous inversion and subsequent misinterpretation. To accurately recover the polarizabilites of a target (parameters that are critical to the success of marine EMI surveys) we have developed two inversion methods that are formulated to take into account sensor positioning errors. One method, named Independent Model Location Inversion (IMLI) [1-2], extends the standard inversion [3] by introducing multiple intermediate sources that attempt to relax the stringent requirement of precise sensor positions. The IMLI algorithm was tested under SERDP MR-2318 for terrestrial applications using MPV data [1-2] as well UltraTEMA marine data collected under ESTCP MR19-5073. The other method, named Joint Estimation of Target and Survey/sensing Parameters (JETSP), is a recent extension of the standard inversion method that intends to explicitly account for sensor positioning errors as unknown perturbations that are to be solved.

In the following, we first provide a brief review of the theoretical background behind EMI sensing and the standard inversion method. Then the IMLI and the JETSP methods are presented in detail. Finally, several examples using UltraTEMA marine data acquired at the Sequim Bay test-site are presented to demonstrate the effectiveness of the proposed methods.

# 2. Data Model

Consider a transient electromagnetic system consisting of transmitting and receiving coils. In active sensing, a primary field emitted from a transmitter illuminates a nearby object and its abrupt change with time induces eddy currents in the metal object. These induced currents produce a transient secondary magnetic field that is measured by a receiver. As a first-order approximation, the low frequency EMI scattering of a metal target can be well represented by an equivalent induced dipole. Mathematically [3], a target is characterized by a 3 × 3 symmetric magnetic polarizability tensor $P(t)$ at time $t$,

$$P(t) = \begin{bmatrix} p_{11}(t) & p_{12}(t) & p_{13}(t) \\ p_{12}(t) & p_{22}(t) & p_{23}(t) \\ p_{13}(t) & p_{23}(t) & p_{33}(t) \end{bmatrix}. \tag{1a}$$

The elements of the tensor $p_{ij}(t)$ represent dipole component in the $i$-th Cartesian direction due to a primary field in the $j$-th Cartesian direction. For the subsequent formulation, the six independent elements in (1a) are arranged as a vector $\mathbf{q}(t)$

$$\mathbf{q}(t) = [p_{11}(t)\ p_{12}(t)\ p_{13}(t)\ p_{22}(t)\ p_{23}(t)\ p_{33}(t)]^{\mathrm{T}}\ , \tag{1b}$$

where the superscript T denotes the transpose operation. The polarizability tensor $P(t)$ in (1a) has an eigen-decomposition,

$$P(t) = \sum_{i=1}^{3} L_i(t)\mathbf{e}_i\mathbf{e}_i^T\ , \tag{2a}$$

where $\mathbf{e}_i$ is the orthonormal eigenvector or Euler vector representing the $i$-th principal direction of dipolar polarization with respect to a reference system. The Euler vector can be determined by a set of three Euler angles that describes the orientation of a dipolar object. $L_i(t)$ is the principal axis polarization strength that is a function of the geometry and material properties of a target. Like the six independent tensor elements, the three principal elements in (2a) are arranged as a vector $\mathbf{f}(t)$ with

$$\mathbf{f}(t) = [L_1(t)\ L_2(t)\ L_3(t)]^{\mathrm{T}}\ . \tag{2b}$$

Assume that a TEM system is deployed in *N* sensing locations, symbolically denoted as $\mathbf{s}$ with an appropriate size, to interrogate the subsurface. For $\eta$ metallic targets present in the sensor field of view, we can express the corresponding measurements $\mathbf{d}(t, \mathbf{s})$ in a vector-matrix notation,

$$\mathbf{d}(t, \mathbf{s}) = \mathrm{A}(\mathbf{r}, \mathbf{s})\mathbf{q}(t) + \mathbf{n}(t)\ , \tag{3}$$

where $\mathbf{d}(t, \mathbf{s})$ has the dimension of *K* x 1. *K* is the number of measurements that are acquired from the *N* sensing locations. For $\eta$ targets, $\mathbf{r}$ contains their locations with the dimension of $3\eta \times 1$ and $\mathbf{q}(t)$ their respective polarizabilities with the dimension of $6\eta \times 1$ (an extension of (1b)). $\mathbf{n}(t)$ is the additive noise vector. $\mathrm{A}(\mathbf{s},\ \mathbf{r})$ is a $K \times 6\eta$ sensitivity matrix that relates the *K* measurements to a given dipole tensor component of each target.

By using (2a)-(2b), we have another vector-matrix expression of the measurements $\mathbf{d}(t, \mathbf{s})$

$$\mathbf{d}(t, \mathbf{s}) = \mathrm{G}(\mathbf{r}, \boldsymbol{\theta}, \mathbf{s})\mathbf{f}(t) + \mathbf{n}(t)\ . \tag{4}$$

In (4), $\boldsymbol{\theta}$ contains the orientations of $\eta$ targets with the dimension of $3\eta \times 1$ and $\mathbf{f}(t)$ their respective principal axis polarizabilities with the dimension$3\eta\times1$ (an extension of (2b)). $\mathrm{G}(\mathbf{r}, \boldsymbol{\theta}, \mathbf{s})$ is an $K \times 3\eta$ sensitivity matrix that relates the *K* measurements to a given dipole principal component of each target.

Equation (3) or (4) models the measurements of an EMI sensor system as the function of target positions/orientations and their polarizabilities as well as sensing locations. Modeling the measurements requires the construction of the sensitivity matrix A or G whose elements involve the Cartesian components of magnetic field vectors at an object's location generated by both receiver and transmitter coils (e.g., see [3]). In the development that follows both formulas will be interchangeably used to estimate the location and orientation of a target and recover its polarizabilities.

# 3. Methods

In a transient electromagnetic (TEM) system, decay responses $\mathbf{d}(t_j, \mathbf{s})$ are usually measured at sensing locations for a series of time instants $t_j, j = 1, \cdots, N_t$. Provided that the number $\eta$ of buried objects is known or assumed, the goal of the inverse problem is to determine the locations, orientations, and principal transient polarizations, i.e., $\left(\mathbf{r}, \boldsymbol{\theta}, \mathbf{f}(t_j)\right)$, that best match the spatial–temporal data $\mathbf{d}(t_j, \mathbf{s})$. Starting from (3) or (4), a full inverse problem may be formulated by minimizing the cost function

$$\min_{\mathbf{r},\mathbf{q}(t_j)} \sum_{j=1}^{N_t} \left\| W_j \left( \mathbf{d}(t_j, \mathbf{s}) - \mathrm{A}(\mathbf{r}|\mathbf{s})\mathbf{q}(t_j) \right) \right\|^2 \tag{5a}$$

or

$$\min_{\mathbf{r},\boldsymbol{\theta},\mathbf{f}(t_j)} \sum_{j=1}^{N_t} \left\| W_j \left( \mathbf{d}(t_j, \mathbf{s}) - \mathrm{G}(\mathbf{r},\boldsymbol{\theta}|\mathbf{s})\mathbf{f}(t_j) \right) \right\|^2 \tag{5b}$$

that is a squared fit measure between the observed data and the predicted ones. $\|\cdot\|$ indicates $L_2$ norm and $W_j$ is a diagonal data weighting matrix for the data at the time $t_j$ . Generally, the elements of this diagonal matrix are chosen to be equal to the inverse of the estimated Gaussian uncertainty for each datum. Throughout this paper, the sensing locations **s** are shown explicitly to emphasize that they are an essential set of the variables on which the measured data and forward model depend. To facilitate the presentation of the methods, from now we change the mathematical notations of the sensitivity matrices with $(\cdot\,|\,\cdot)$. For example, the left part in the bar of $\mathrm{A}(\mathbf{r}|\mathbf{s})$ or $\mathrm{G}(\mathbf{r},\boldsymbol{\theta}|\mathbf{s})$ of (5) is meant as model parameters that are to be optimized and the right part as variables that remain unchanged or fixed. That is, in this formulation setup, the sensing locations **s** are not the part of the model parameters.

The inversion with (5a) or (5b) is mathematically simple, but its implementation may be numerically problematic. For example, the magnitude of tensor polarizations $\mathbf{q}(t_j)$ have a large dynamic range and their estimation depends on the unknown locations $\mathbf{r}$. Determining parameters $\mathbf{r}$, $\mathbf{q}(t_j)$ simultaneously can make the problem severely ill-posed and requires a careful weighting for different scale sensitivity sub-matrices. Also, it is more difficult to make an educated initial guess for polarizations than for source location. The same numerical issues also hold for (5b) when attempting to solve the parameters $\left(\mathbf{r}, \boldsymbol{\theta}, \mathbf{f}(t_j)\right)$ all at once.

## 3.1 Standard inversion procedure

Notice that, from (3)-(4), the EMI response is linear with respect to dipolar polarization and nonlinear with respect to the locations and/or orientations of objects. By making use of this fact, we group our model parameters into two classes: a nonlinear part consisting of source locations **r** or orientations $\boldsymbol{\theta}$ and a linear part consisting of source tensor $\mathbf{q}(t_j)$ or principal-axis $\mathbf{f}(t_j)$ polarizations. Referring to (3) or (4), we say that the two parameter sets are separable since the matrix $\mathrm{A}(\mathbf{r}, \mathbf{s})$ or $\mathrm{G}(\mathbf{r}, \boldsymbol{\theta}, \mathbf{s})$ is independent of source polarizations $\mathbf{q}(t_j)$ or $\mathbf{f}(t_j)$. By using this separable property, our inversion algorithms are designed to treat two parameter classes separately and recursively. In the other words, source locations are found as a primary step and tensor or principal polarizations are estimated as an intermediate, embedded step during the iteration. These steps are elaborated in the following.

Given a set of starting or current locations $\mathbf{r}_c$, first we solve a constrained linear optimization problem for the polarization

$$\tilde{\mathbf{q}}(t_j) = \underset{\mathbf{q}(t_j)}{\operatorname{argmin}} \left\| \mathbf{d}(t_j, \mathbf{s}) - \mathbf{A}(\mathbf{r}_c|\mathbf{s})\mathbf{q}(t_j) \right\|^2, \text{ s. t. } \mathbf{q}(t_j) \in S^+ , \tag{6}$$

where $\tilde{\mathbf{q}}(t_j)$ denotes the estimated the tensor polarization at time channel $t_j$. $\mathbf{q}(t_j) \in S^+$ constrains that $\mathbf{q}(t_j)$ is sought to be the elements of the set $S^+$ of symmetric positive semi-definite matrices (Song et al, 2011). Then the target locations $\mathbf{r}_c$ are updated by minimizing the following objective function

$$\tilde{\mathbf{r}} = \underset{\mathbf{r}}{\operatorname{argmin}} \sum_{i=1}^{N_t} \left\| W_j \left( \mathbf{d}(t_j, \mathbf{s}) - \mathbf{A}(\mathbf{r}_c|\mathbf{s})\tilde{\mathbf{q}}(t_j) \right) \right\|^2, \text{ s.t. } \|\mathbf{r} - \mathbf{r}_c\| \le \Delta_{\mathbf{r}} , \tag{7}$$

where $\tilde{\mathbf{r}}$ denotes the estimated target locations. $\Delta_{\mathbf{r}}$ is a positive scalar used to provide a local ball within which $\mathbf{r}$ is allowed to change w.r.t. $\mathbf{r}_c$ in the algorithm. Generally, the location searches can be conducted within specified bounds. As the calculation of the predicted data requires that $\tilde{\mathbf{q}}(t_j)$ be evaluated, the solution of (6) can be implemented as an embedded process in (7). Algorithmically, the steps defined in (6) and (7) are iterated until convergence criteria are satisfied and the final set of locations and tensor polarizations $\left(\tilde{\mathbf{r}}, \tilde{\mathbf{q}}(t_j)\right)$ are yielded. Afterwards, the principal polarizabilities $L_i(t_j)$ of each object can be obtained through the eigendecomposition (2a) of the estimated $\tilde{P}(t_j)$, which is the polarizability tensor re-arranged from $\tilde{\mathbf{q}}(t_j)$. The orientation of each object can be estimated in terms of the corresponding Euler vector, which is determined by the joint diagonalization of $\tilde{P}(t_j)$ across a range of times [3].

Upon the solution obtained in steps of (6) and (7), the orientation and principal polarizabilities may be further optimized with formulation (4). By fixing the object locations at $\tilde{\mathbf{r}}$ and starting from the current estimate of orientations $\boldsymbol{\theta}_c$ of targets derived from the joint diagonalization method, $\mathbf{f}(t_j)$ is evaluated with the similar process of finding $\mathbf{q}(t_j)$ in the location search. That is, we solve the linear sub-problem by minimizing

$$\tilde{\mathbf{f}}(t_j) = \underset{\mathbf{f}(t_j)}{\operatorname{argmin}} \left\| \mathbf{d}(t_j, \mathbf{s}) - \mathbf{G}(\boldsymbol{\theta}_c|\tilde{\mathbf{r}}, \mathbf{s})\mathbf{f}(t_j) \right\|^2, \text{ s. t. } \mathbf{f}(t_j) \ge \mathbf{0} , \tag{8}$$

where $\tilde{\mathbf{f}}(t_j)$ denotes the estimated principal polarizabilities at time channel $t_j$. Analogous to the case of finding the locations of the objects in (7), the current orientations $\boldsymbol{\theta}_c$ are updated by minimizing the objective function

$$\tilde{\boldsymbol{\theta}} = \underset{\mathbf{r}}{\operatorname{argmin}} \sum_{i=1}^{N_t} \left\| W_j \left( \mathbf{d}(\mathbf{s}, t_j) - \mathbf{G}(\boldsymbol{\theta}_c|\tilde{\mathbf{r}}, \mathbf{s})\tilde{\mathbf{f}}(t_j) \right) \right\|^2, \text{ s.t. } \|\boldsymbol{\theta} - \boldsymbol{\theta}_c\| \le \Delta_{\boldsymbol{\theta}} \tag{9}$$

$\Delta_{\boldsymbol{\theta}}$ is a positive scalar representing the trust region size internally used in the algorithm (see reference in Song et al, 2011). Similarly, the solution process of (8) is implemented as a nested linear inversion in (9) and is used to generate the predicted data. Also, the steps defined in (8) and (9) are iterated until convergence criteria are satisfied and the final solution set is given as the locations, orientations, and principal polarizations $\left(\tilde{\mathbf{r}}, \tilde{\boldsymbol{\theta}}, \tilde{\mathbf{f}}(t_j)\right)$. Finally, either both solutions of (6)-(7) and (8)-(9) are kept in the classification stage or one solution, with the better data fit, is chosen. This completes the description of the standard inversion algorithm.

## 3.2 Independent Model Location Inversion: sensor point of view

When implementing the standard inversion method, all data from $N$ sensing locations can be organized arbitrarily. But the most natural way of organizing data may be based on the sensing locations. Re-express the symbolic notation $\mathbf{s}$ of $N$ sensing locations as $\mathbf{s} = [\mathbf{s}_1; \cdots; \mathbf{s}_n; \cdots; \mathbf{s}_N]$. Then we may group data into the form

$$\mathbf{d}(t_j, \mathbf{s}) = [\mathbf{d}_1(t_j, \mathbf{s}_1); \cdots; \mathbf{d}_n(t_j, \mathbf{s}_n);\ \cdots;\ \mathbf{d}_N(t_j, \mathbf{s}_N)]. \tag{10}$$

Corresponding to (10), the sensitivity matrix in the forward operation of the standard method can be expanded as

$$\mathrm{G}(\mathbf{r}, \boldsymbol{\theta}|\mathbf{s}) = [\mathrm{G}_1(\mathbf{r}, \boldsymbol{\theta}|\mathbf{s}_1); \cdots;\ \mathrm{G}_n(\mathbf{r}, \boldsymbol{\theta}|\mathbf{s}_n);\ \ \cdots;\ \mathrm{G}_N(\mathbf{r}, \boldsymbol{\theta}|\mathbf{s}_N)]. \tag{11}$$

Note that in the above we use Matlab notation ; to denote the row-stacking operation on either column vectors or matrices. As evident in (11), the sensing locations in the standard inversion procedure are treated as the known quantities and are not included in the optimization process.

What is implied in (11) is that, in the user frame of reference, all sensors placed at different locations $\mathbf{s}_n (n = 1, \cdots, N)$ would "see" the presence of targets at the same locations and orientations denoted as $(\mathbf{r}, \boldsymbol{\theta})$. In principle, this sensor-view assumption can be satisfied only under the conditions that the sensor locations are precisely known or have small positional errors. For the case of inaccurate sensor positioning, it becomes difficult with the standard algorithm to generate one set of target locations and orientations that are guaranteed to be close to the true solutions under all $N$ sensing views. As a result, the standard method is likely to generate a poor estimate of the polarizabilities.

To deal with the requirement of precise sensing locations, we may relax the stringent, unitary view of all sensors to targets that is imposed in the standard method. Imagine the sensors deployed in the $n$-th sensing location $\mathbf{s}_n$ "view" the targets as if they were at $(\mathbf{r}_n,\ \boldsymbol{\theta}_n)$, not necessarily at the desired, true locations $\mathbf{r}$ and orientations $\boldsymbol{\theta}$. $(\mathbf{r}_n,\ \boldsymbol{\theta}_n)$ may be called the perturbed version of $(\mathbf{r},\ \boldsymbol{\theta})$ with the associated perturbations $(\Delta\mathbf{r}_n,\ \Delta\boldsymbol{\theta}_n)$ that are attributed to the positional errors of the $n$-th sensing location. With this line of reasoning, we say that the target locations and orientations viewed from the $n$-th sensing location are $\mathbf{r}_n = \mathbf{r} + \Delta\mathbf{r}_n$ and $\boldsymbol{\theta}_n = \boldsymbol{\theta} + \Delta\boldsymbol{\theta}_n$. Substituting $(\mathbf{r},\ \boldsymbol{\theta})$ with $(\mathbf{r}_n,\ \boldsymbol{\theta}_n)$ in (11) leads to a modified form

$$\mathrm{G}(\mathbf{r}_n, \boldsymbol{\theta}_n, n = 1, \cdots, N|\mathbf{s}) = [\mathrm{G}_1(\mathbf{r}_1, \boldsymbol{\theta}_1|\mathbf{s}_1);\ \cdots;\ \mathrm{G}_n(\mathbf{r}_n, \boldsymbol{\theta}_n|\mathbf{s}_n);\ \ \cdots;\ \mathrm{G}_N(\mathbf{r}_N, \boldsymbol{\theta}_N|\mathbf{s}_N)]. \tag{12}$$

The distinction between (11) and (12) looks clear. In (11) all the sub-matrices $\mathrm{G}_n$ are constructed with a single set of source locations and orientations $(\mathbf{r}, \boldsymbol{\theta})$, while in (12) each sub-matrix $\mathrm{G}_n$ is constructed with a different set of source locations and orientations $(\mathbf{r}_n,\ \boldsymbol{\theta}_n), n = 1, \cdots, N$. Figure 1(a) schematically shows the concept behind (12).. In the figure, a projectile shaped target at $\mathbf{r}$ is sensed by an array of sensors deployed at two positions $\mathbf{s}_1$ and $\mathbf{s}_2$ (the two parallelograms with solid lines). From the perspective of each sensing location, the target would be "seen" as if they are present at $\mathbf{r_1} = \mathbf{r} + \Delta\mathbf{r_1}$ and $\mathbf{r_2} = \mathbf{r} + \Delta\mathbf{r_2}$ (the dash-outlined projectile shape) as well as with the two orientations, respectively. For clarity, only the two locations are notated.

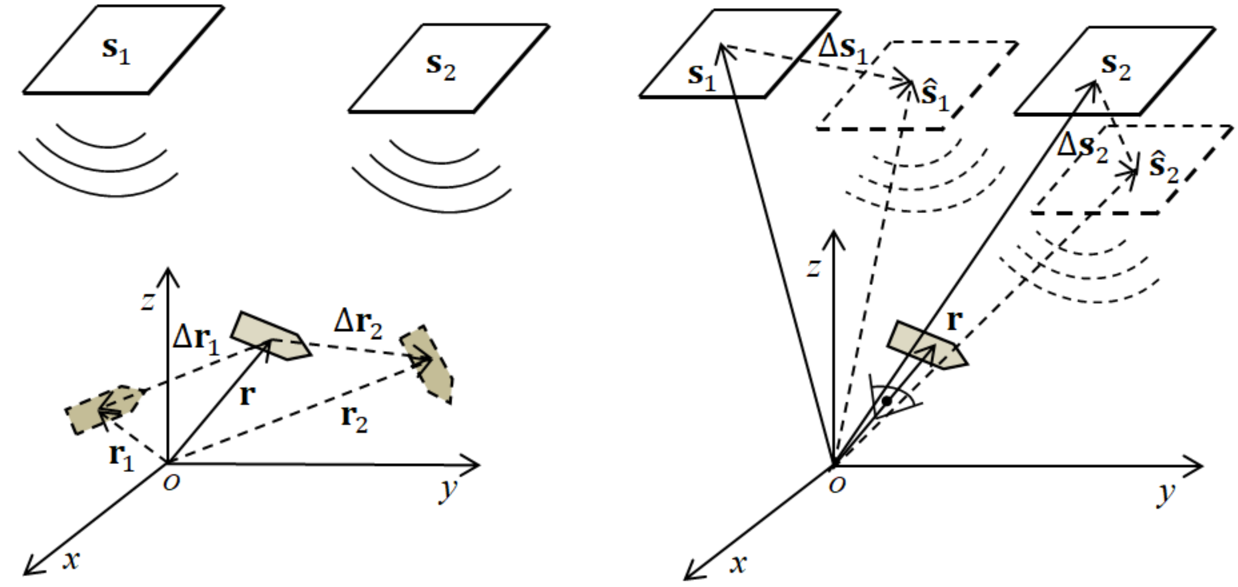

(a) (b)

**Figure 1**. Conceptual description of the two methods. A projectile shape with a solid outline represents a target located at $\mathbf{r}$ sensed by an array of sensors at two nominal positions denoted as $\mathbf{s}_1$ and $\mathbf{s}_2$ (the two parallelograms with solid lines) (a) IMLI. The two soundings "see" the target at $\mathbf{r_1} = \mathbf{r} + \Delta\mathbf{r_1}$ and $\mathbf{r_2} = \mathbf{r} + \Delta\mathbf{r_2}$ (the depicted projectile shape with a dashed outline) as well as with the two orientations, respectively. For clarity, only the two locations are notated. (b) JETSP. The target to be "seen" at $\mathbf{r}$ "requires" correcting the nominal sensing positions as $\hat{\mathbf{s}}_\mathbf{1} = \mathbf{s_1} + \Delta\mathbf{s_1}$ and $\hat{\mathbf{s}}_\mathbf{2} = \mathbf{s_2} + \Delta\mathbf{s_2}$ (the two parallelograms with dashed lines), respectively.

With this data grouping, each set of extrinsic source parameters are attached to one sensing location that is independent of each another. Meanwhile, related to these $N$ sets of extrinsic source parameters in (12) are the principal polarizabilities $\mathbf{f}(t_j)$ as defined in (2b) or (4). Recall that the principal polarizabilities describe the physical properties of targets and are invariant with respect to the perturbed placement of sensors. As in the standard method, they are constrained to be common within the field of view of all soundings. This derives the independent model location inversion. For the case of accurate sensor positioning that theoretically leads to small perturbations of $(\Delta\mathbf{r}_n,\ \Delta\boldsymbol{\theta}_n)$, the perturbed $(\mathbf{r}_n,\ \boldsymbol{\theta}_n)$ introduced in the IMLI method would be the same or close to the true $(\mathbf{r},\ \boldsymbol{\theta})$, then the IMLI reduces to the standard inversion method. Following the implementation of the standard inversion method in (8) and (9), we carry out the IMLI as follows.

Upon obtaining the solution through steps of (6) - (9), we assign the current object locations and orientations $\mathbf{r}_\mathrm{c}$ and $\boldsymbol{\theta}_\mathrm{c}$ into the $N$ sets of independent source locations and orientations $\mathbf{r}_{\mathrm{c},n}$ and $\boldsymbol{\theta}_{\mathrm{c},n}$ $(n = 1, \cdots, N)$. For simplified notation, we set the extrinsic parameters as $\mathbf{m}_{\mathrm{c},n} = [\mathbf{r}_{\mathrm{c},n};\ \boldsymbol{\theta}_{\mathrm{c},n}]$ and note that $\mathbf{f}(t_j)$ will be evaluated through equation (8) with a small modification. The sensitivity matrix G $(\mathbf{r}_\mathrm{c},\ \boldsymbol{\theta}_\mathrm{c}|\mathbf{s})$ in (8) is replaced with G $(\mathbf{m}_{\mathrm{c},n}, n = 1, \cdots, N|\mathbf{s})$ of (12). Different from the case of finding the source locations and orientations in the standard method, the $N$ sets of current extrinsic source parameters $\mathbf{m}_{\mathrm{c}} = [\mathbf{m}_{\mathrm{c},1}; \cdots; \mathbf{m}_{\mathrm{c},n}; \cdots; \mathbf{m}_{\mathrm{c},n}]$ are simultaneously updated by minimizing the function

$$\tilde{\mathbf{m}} = \underset{\mathbf{m}}{\operatorname{argmin}} \sum_{i=1}^{N_t} \left\| W_j \left( \mathbf{d}(\mathbf{s}, t_j) - \mathbf{G}(\mathbf{m}_{\mathrm{c},n},\ n = 1, \cdots, N|\mathbf{s}) \tilde{\mathbf{f}}(t_j) \right) \right\|^2,\ \text{s.t.}\ \|\mathbf{m} - \mathbf{m}_{\mathrm{c}}\| \le \Delta_{\mathbf{m}}\ , \tag{13}$$

where $\Delta_{\mathbf{m}}$ is a positive scalar representing the trust region size internally used in the algorithm. Then the linear sub-problem nested in (13) is solved by minimizing

$$\tilde{\mathbf{f}}(t_j) = \underset{\mathbf{f}(t_j)}{\operatorname{argmin}} \left\| \mathbf{d}(\mathbf{s}, t_j) - \mathbf{G}(\mathbf{m}_{\mathrm{c},n},\ n = 1, \cdots, N|\mathbf{s}) \mathbf{f}(t_j) \right\|^2,\ \text{s.t.}\ \mathbf{f}(t_j) \ge \mathbf{0}\ . \tag{14}$$

Again, the estimated principal polarizabilities $\tilde{\mathbf{f}}(t_j)$ at time channel $t_j$ are common for all subsets of data $\mathbf{d}(\mathbf{s}, t_j) = [\mathbf{d}_1(\mathbf{s}_1, t_j); \cdots; \mathbf{d}_n(\mathbf{s}_n, t_j); \cdots; \mathbf{d}_N(\mathbf{s}_N, t_j)]$ while $\mathbf{m}_{\mathrm{c},n}$ are allowed to be different. Like the standard inversion algorithm, iterating the steps defined in (13) and (14) concludes when the stopping criteria are met. The estimated solution includes the $N$ sets of independent, extrinsic source parameters and the principal polarizations $\left(\tilde{\mathbf{m}},\ \tilde{\mathbf{f}}(t_j)\right)$. These $N$ sets of perturbed source locations are intermediate in the sense that they are only used to account for the sensor positioning errors, whereas the estimated principal polarizabilities $\tilde{\mathbf{f}}(t_j)$**,** which are expected to be more accurate, are retained as the final ones $\tilde{\mathbf{f}}_{\mathrm{IMLI}}(t_j)$. To determine one final set of source locations, we fix $\tilde{\mathbf{f}}_{\mathrm{IMLI}}(t_j)$ and take the average over the $N$ sets of estimated independent source locations and orientations as a set of starting points. The starting or current points $(\mathbf{r}_c, \boldsymbol{\theta}_c)$ are then updated by solving the following nonlinear optimization problem,

$$\begin{gathered} (\tilde{\mathbf{r}}, \tilde{\boldsymbol{\theta}}) = \underset{(\mathbf{r},\boldsymbol{\theta})}{\operatorname{argmin}} \sum_{i=1}^{N_t} \left\| W_j \left( \mathbf{d}(t_j, \mathbf{s}) - \mathbf{G}(\mathbf{r}_{\mathrm{c}}, \boldsymbol{\theta}_{\mathrm{c}}|\mathbf{s}) \tilde{\mathbf{f}}_{\mathrm{IMLI}}(t_j) \right) \right\|^2 \\ \text{subject to } (\|\mathbf{r} - \mathbf{r}_{\mathrm{c}}\|, \|\boldsymbol{\theta} - \boldsymbol{\theta}_{\mathrm{c}}\|) \le (\Delta_{\mathbf{r}},\ \Delta_{\boldsymbol{\theta}}) \end{gathered} \tag{15}$$

Combing the steps defined in (13)-(15)), we generate the IMLI solution set $\left(\tilde{\mathbf{r}}_{\mathrm{IMLI}}, \tilde{\boldsymbol{\theta}}_{\mathrm{IMLI}}, \tilde{\mathbf{f}}_{\mathrm{IMLI}}(t_j)\right)$ that are the target locations, orientations, and principal polarizations. A flow diagram of the IMLI algorithm is given in Figure 2.

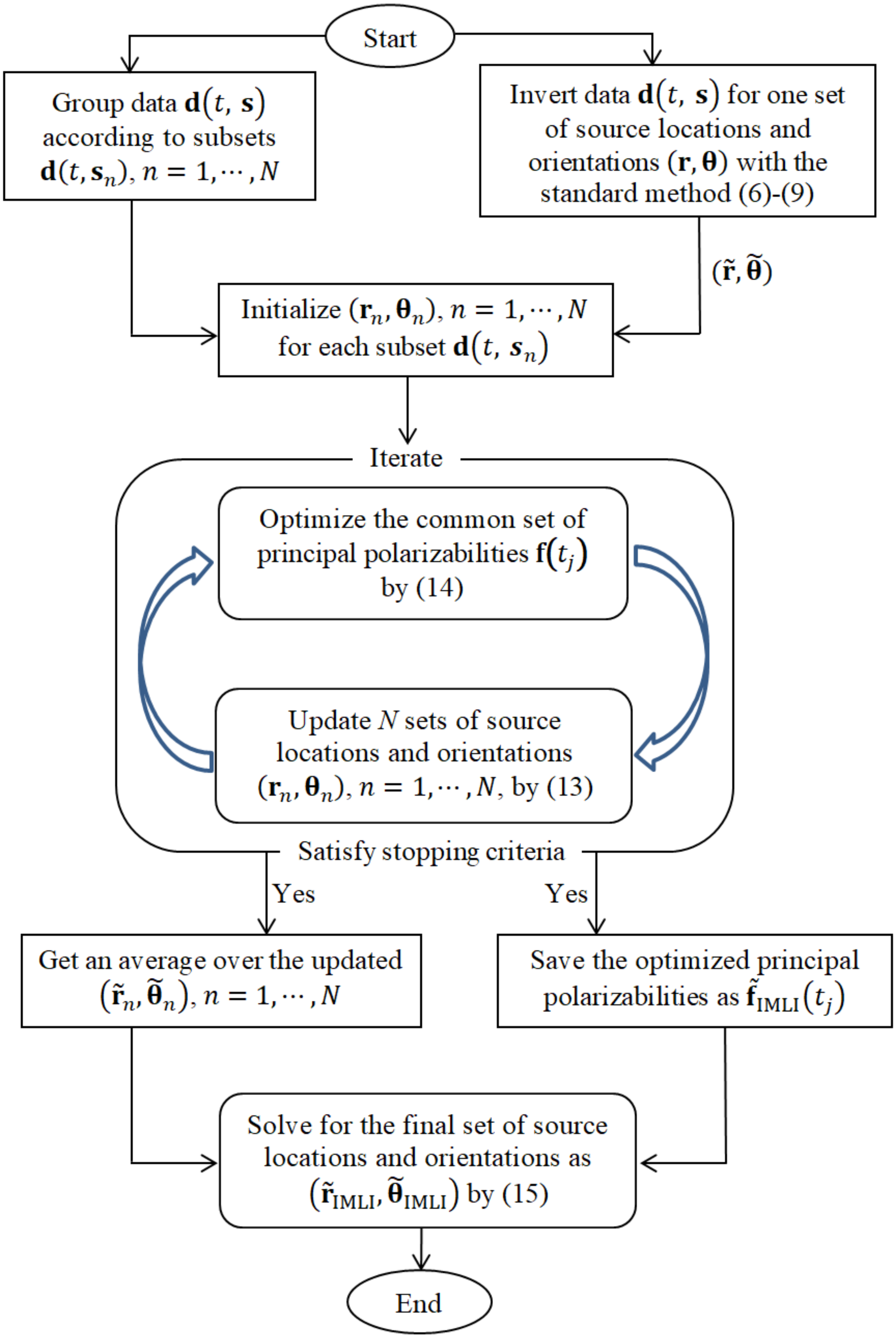

**Figure 2.** Flow diagram of the IMLI method.

## 3.3 Joint estimation of target and survey parameters: target point of view

As described in section 3.2, the IMLI method implicitly accounts for the sensor positional uncertainty by introducing $N$ independent model locations $(\mathbf{r}_n,\ \boldsymbol{\theta}_n), \boldsymbol{n} = \mathbf{1}, \cdots, \boldsymbol{N}$ that are tied to each individual sensing location. This is a sensing perspective from which multiple projected source locations, deviated from the true locations of targets, can be present. If the sensing viewpoint is switched to the target's perspective an alternative method for accounting for sensor positioning errors can be formulated. In this reversed process the recorded sensing locations are adjusted from the target's perspective. The measurement at a nominal position $\boldsymbol{s}_n$ requires an adjustment $\Delta\boldsymbol{s}_n$ so that the adjusted sensing locations $\hat{\mathbf{s}}_n = \mathbf{s}_n + \Delta\boldsymbol{s}_n$ can harmonize with the actual geometrical presence $(\mathbf{r},\ \boldsymbol{\theta})$ of targets. The idea of this formulation is graphically shown in Figure 1(b). In common with the set up in Figure 1(a), an array of sensors is deployed at two positions $\mathbf{s}_1$ and $\mathbf{s}_2$ (the two parallelograms with solid lines) and used to interrogate a projectile shaped target located at $\mathbf{r}$. In the Figure, the corrected nominal sensing positions marked as $\hat{\mathbf{s}}_1 = \mathbf{s}_1 + \Delta\boldsymbol{s}_1$ and $\hat{\mathbf{s}}_2 = \mathbf{s}_2 + \Delta\boldsymbol{s}_2$ (the two parallelograms with dashed lines) are required to "see" the target that is present at $\mathbf{r}$ from the correct sensing perspective.

For this target viewpoint, we introduce the sensing location perturbations $\Delta\boldsymbol{s}_n$ as unknowns that are additional to source parameters $(\mathbf{r},\ \boldsymbol{\theta})$. Thus, the method of joint estimation of target and survey/sensing parameters is proposed.

Set $\Delta\mathbf{s} = [\Delta\mathbf{s}_1; \cdots; \Delta\mathbf{s}_n; \cdots; \Delta\mathbf{s}_N]$. With the grouped data in (10) and the sensing location perturbations $\Delta\mathbf{s}$, the sensitivity matrix A $(\mathbf{r}|\mathbf{s})$ appeared in the standard method is modified as

$$\mathrm{A}(\mathbf{r},\ \Delta\mathbf{s}|\mathbf{s}) = [\mathrm{A}_1(\mathbf{r},\ \Delta\mathbf{s}_1|\mathbf{s}_1); \cdots;\ \mathrm{A}_n(\ \mathbf{r},\ \Delta\mathbf{s}_n|\mathbf{s}_n);\ \ \cdots;\ \mathrm{A}_N(\mathbf{r},\ \Delta\mathbf{s}_N|\mathbf{s}_N)]. \tag{16}$$

Starting from the standard solution locations $\tilde{\mathbf{r}} = \mathbf{r}_\mathrm{c}$ and initializing $\Delta\boldsymbol{s}_c$, we solve a constrained linear optimization problem for the polarization

$$\hat{\mathbf{q}}(t_j) = \underset{\mathbf{q}(t_j)}{\operatorname{argmin}} \left\| \mathbf{d}(\mathbf{s}, t_j) - \mathbf{A}(\mathbf{r}_\mathrm{c}, \Delta\mathbf{s}_\mathrm{c}|\mathbf{s})\mathbf{q}(t_j) \right\|^2,\ \text{s. t. } \mathbf{q}(t_j) \in S^+, \tag{17}$$

where $\hat{\mathbf{q}}(t_j)$ denotes the estimated tensor polarizabilities that are constrained to belong to the class of symmetric positive semi-definite matrices. Then, the target locations $\mathbf{r}_\mathrm{c}$ and sensing location perturbations $\Delta\boldsymbol{s}_\mathrm{c}$ are updated by minimizing the following objective function

$$\begin{gathered}(\hat{\mathbf{r}}, \widehat{\Delta\mathbf{s}}) = \underset{(\mathbf{r},\ \Delta\mathbf{s})}{\operatorname{argmin}} \sum_{i=1}^{N_t} \left\| W_j \left( \mathbf{d}(\mathbf{s}, t_j) - \mathbf{A}(\mathbf{r}_\mathrm{c}, \Delta\mathbf{s}_\mathrm{c}|\mathbf{s}) \hat{\mathbf{q}}(t_j) \right) \right\|^2 \\ \text{subject to } (\|\mathbf{r} - \mathbf{r}_\mathrm{c}\|,\ \|\Delta\mathbf{s} - \Delta\mathbf{s}_\mathrm{c}\|) \le (\Delta_\mathbf{r},\ \Delta_{\Delta\mathbf{s}})\end{gathered} \tag{18}$$

where $\hat{\mathbf{r}}$ and $\widehat{\Delta\mathbf{s}}$ denote the estimated target locations and sensing location perturbations. $\Delta_\mathbf{r}$ and $\Delta_{\Delta\mathbf{s}}$ are the positive scalars used to provide a local ball within which $\mathbf{r}$ and $\Delta\mathbf{s}$ are allowed to change w.r.t. $\mathbf{r}_\mathrm{c}$ and $\Delta\boldsymbol{s}_\mathrm{c}$ in the algorithm. The implementation of the JETSP algorithm is much like that of the standard inversion method. The execution of (17), which is an embedded process in (18), includes the evaluation of $\hat{\mathbf{q}}(t_j)$ and generation of the predicted data. The final set of locations and tensor polarizations $(\hat{\mathbf{r}}, \hat{\mathbf{q}}(t_j), \widehat{\Delta\mathbf{s}})$ are yielded upon convergence of the iterative process within (17) and (18). By recasting the estimated tensor elements $\hat{\mathbf{q}}(t_j)$ into the tensor

$\hat{P}(t_j)$, the principal polarizabilities of targets, denoted as $\hat{\mathbf{f}}(t_j)$, can be obtained through the eigen-decomposition (2a). It follows that the orientation of each object is estimated from the Euler vector associated with the joint diagonalized matrices of $\hat{P}(t_j)$ across a range of times.

We continue to optimize the orientation and the principal axis polarizabilities. In this step, we fix the object locations at $\hat{\mathbf{r}}$ and use the adjusted sensing locations $\hat{\mathbf{s}} = \mathbf{s} + \widehat{\Delta\mathbf{s}}$ that are obtained by solving the problem of (17) and (18). Beginning with the current estimate of orientations $\boldsymbol{\theta}_\mathrm{c}$ of targets derived from the joint diagonalization process, the evaluation of $\mathbf{f}(t_j)$ is performed by solving the linear inverse problem

$$\bar{\mathbf{f}}(t_j) = \underset{\mathbf{f}(t_j)}{\operatorname{argmin}} \left\| \mathbf{d}(\mathbf{s}, t_j) - \mathrm{G}(\boldsymbol{\theta}_c, \hat{\mathbf{r}},\ \hat{\mathbf{s}})\mathbf{f}(t_j) \right\|^2,\ \text{s. t. } \mathbf{f}(t_j) \geq \mathbf{0}\ , \tag{19}$$

where $\bar{\mathbf{f}}(t_j)$ is the estimated principal polarizabilities at time channel $t_j$. Analogous to the case of jointly finding the target locations and the sensing location perturbations in (18), the current orientations $\boldsymbol{\theta}_\mathrm{c}$ are updated by solving the following nonlinear optimization problem:

$$\hat{\boldsymbol{\theta}} = \underset{\boldsymbol{\theta}}{\operatorname{argmin}} \sum_{i=1}^{N_t} \left\| W_j \left( \mathbf{d}(\mathbf{s}, t_j) - \mathrm{G}(\boldsymbol{\theta}_\mathrm{c} | \hat{\mathbf{r}}, \hat{\mathbf{s}}) \bar{\mathbf{f}}(t_j) \right) \right\|^2,\ \text{s.t. } \|\boldsymbol{\theta} - \boldsymbol{\theta}_\mathrm{c}\| \leq \Delta_{\boldsymbol{\theta}}\ , \tag{20}$$

where $\Delta_{\boldsymbol{\theta}}$ is a positive scalar representing the trust region size internally used in the algorithm. As with the standard method, the solution process of (19) is treated as a nested linear inversion in (20) and is used to generate the predicted data. As usual, the iterations of (19) and (20) are continued until a pre-defined tolerance criterion is satisfied. At the final step the JETSP algorithm outputs the solution set, including the locations, orientations, and the principal polarizations, either $\left(\hat{\mathbf{r}}_\mathrm{JETSP}, \hat{\boldsymbol{\theta}}_\mathrm{JETSP}, \hat{\mathbf{f}}_\mathrm{JETSP}(t_j)\right)$ or $\left(\hat{\mathbf{r}}_\mathrm{JETSP}, \bar{\boldsymbol{\theta}}_\mathrm{JETSP}, \bar{\mathbf{f}}_\mathrm{JETSP}(t_j)\right)$ or both.

This completes the description of the method of joint estimation of target and sensing parameters. Figure 2 shows a flow diagram of implementing the JETSP method.

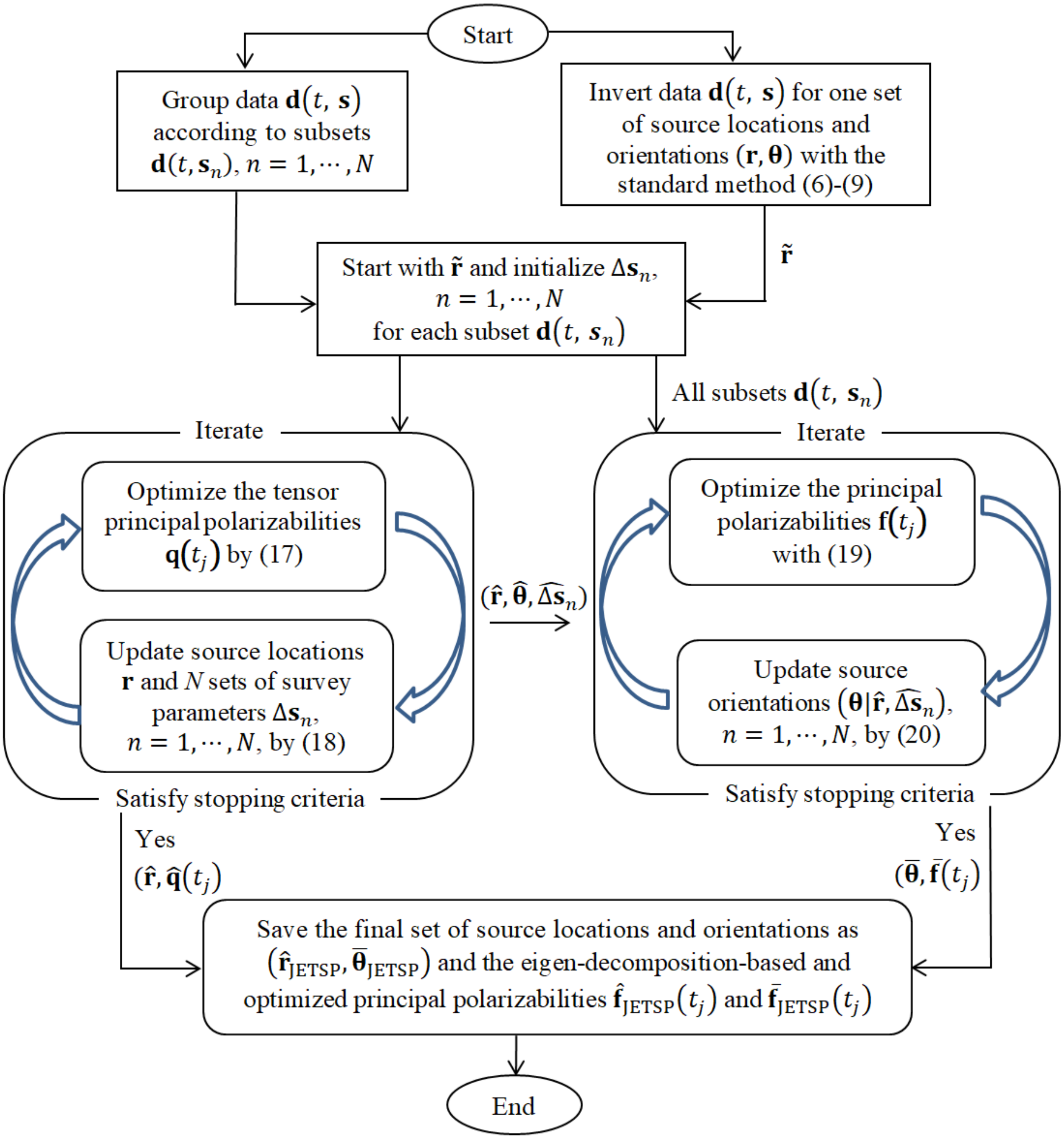

**Figure 3.** Flow diagram of JETSP method.

# 4. Results

Our initial development and experiences with the IMLI method were obtained on multishot cued and dynamic surveys in terrestrial environments [1-2]. Here we consider the application of the IMLI and JETSP methods to inverting the marine UltraTEMA data acquired at the Sequim Bay demonstration site under ESTCP MR19-5073. The UltraTEMA [4] is a multi-component multistatic system installed on a submersible tow-fish. The UltraTEMA comprises four horizontally arranged transmitters and twelve three-component receiver cubes, shown in Figure 4. Three transmitters have a sensor footprint size of 1.8 m × 1.8 m, while the fourth transmitter is rectangular with a size of 3.6 m × 0.9 m. The transmitter on the system can be operated in either fast (90 Hz base-frequency) or slow (30 Hz base-frequency) modes. The data presented below were acquired in the fast-transmitter mode with $N_t$= 27 logarithmically spaced gates between 0.124 ms and 2.42 ms. For each transmitter excitation, UltraTEM records the response at all receivers. Thus, it has spatial–temporal data of 144 × $N_t$ for a survey point.

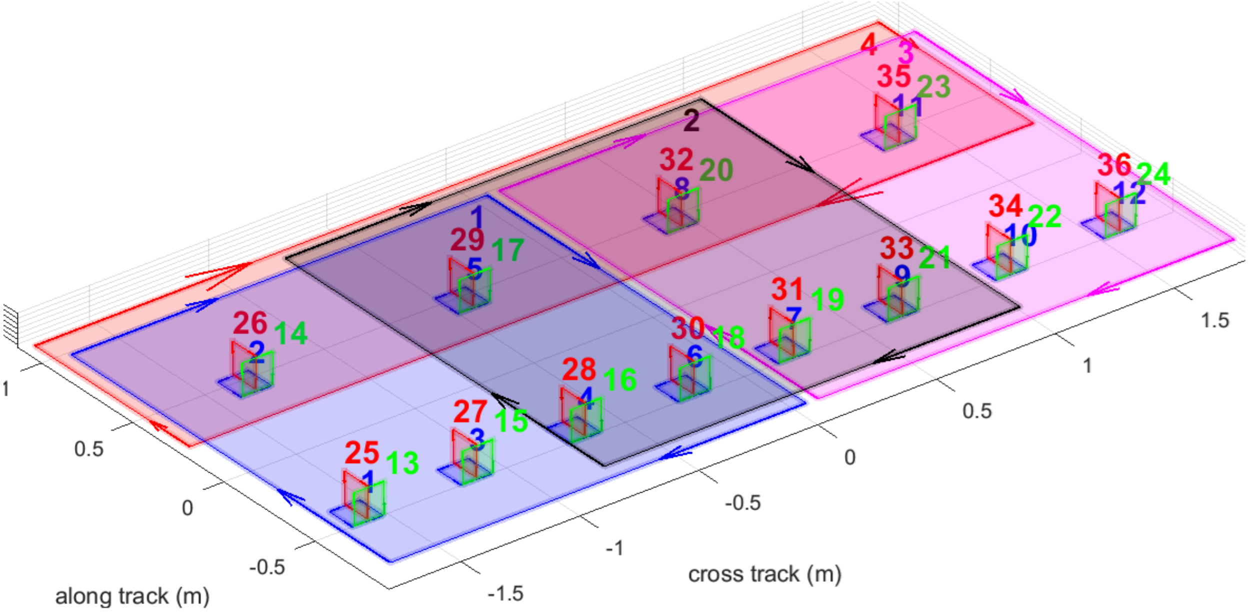

**Figure 4.** Marine UltraTEM: A multicomponent system consisting of four horizontally arranged transmitters and twelve triaxial receiver cubes.

Applying the IMLI and the JETSP methods require the data to be grouped with sensing locations. The term "sensing locations" is loosely used in this context. Its concrete definition or specification depends upon what a kind of survey is conducted. For a cued survey, there may be a few shots that are placed over an area of interest and the cued data can be grouped by shot number. A marine EMI survey is typically operated in a continuous, dynamic mode that generates numerous shots along a single pass. Often, there are multiple passes conducted to ensure good coverage over the area of interest. To effectively implement the IMLI and JETSP methods in the inversion of underwater data, we assume that each survey line shares the same relative positional offset and group the data and set up the model parameters accordingly.

Next, we will demonstrate the performance of the methods using several examples with the data acquired on the calibration and blind grid sites at Sequim Bay in October 2021 and September 2022.

### *Calibration data examples*

Before proceeding with an inversion of EMI data, target detection is performed on a data image that was created by combing z-component data of all transmitters. An anomaly blob on the data map, which has maximum amplitude exceeding a threshold, is identified and picked as a target [4]. Figure 5 shows a 4 m x 4 m area where there are three survey passes represented by the dotted colored lines (cyan, orange, and blue). In the figure, each line of dots denotes the track of one of the receiver cubes during a given pass. Within the solid black circle centered on the target picking location, the data are selected and inverted. The source locations derived from the standard, IMLI, and JETSP methods are marked as the red circle, diamond, and square, respectively, and also presented in each plot of recovered polarizabilities (Figure 6). The observed and predicted responses and residuals are shown in Figure 7. Top row is for the standard inversion, middle the IMLI, and bottom JETSP. One can see that large residuals remain in the standard method, whereas the IMLI and the JETSP are able to more accurately fit the observed data. In this example, both IMLI and JETSP methods recover polarizabilites that agree well with those of the ground-truth (105mm projectile) with polarizability matching misfist of 0.206, 0.284. The standard inversion returns polarizabilities that exhibit no symmetry with a large matching misfit of 1.337. A point of interest here is to compare the inverted source locations between the IMLI and JETSP. The standard method and IMLI give the source locations at (0.17, -0.40, -1.20) m and (0.18, -0.33, -1.02) m, respectively. Both source locations are close horizontally but with a depth difference of 18 cm. On the other hand, the JETSP has the inverted source at (0.57, -0.39, -1.11) m. The major location difference between the IMLI and the JETSP is in the x-coordinate. The source in the JETSP is shifted toward the east 40 cm relative to the sources in the other two methods. At present, it is unclear what factors can cause such a difference. It could be an algorithmic issue within our Matlab formulation or something else related to the data. This will be investigated further.

In the second example, we show a case of recovering the polarizabilities from a 60mm mortar. In this case, the survey map of Figure 8 shows that there are four survey lines (marked as dotted colored lines, cyan, orange, blue, and purple) contained in the 4 m x 4 m section area. Again, the masked data within the black circle are inverted. The source locations derived from the three methods, the standard (red circle), IMLI (diamond), and the JETSP (square), are given as (0.22, 0.27, -0.61) m, (0.23, 0.28, -0.67) m, and (0.23, 0.31, -0.62) m, respectively. Figure 10 presents the observed and predicted responses and residuals. Similar to the case illustrated in Figure 5, the standard method has some difficulty fitting the observed data and results large residuals that are not explained by the model. Comparatively, the residuals from the IMLI and the JETSP are seen to be much smaller. When inspecting the recovered polarizabilities shown in Figure 9, we see that the standard inversion obtains primary and secondary polarizabilities that are close to the ground-truth ones, but the tertiary one has a systematic offset compared to the reference. Overall, the standard method has a polarizability matching misfit of 0.512. In contrast, both IMLI and JETSP methods are able to deliver significantly improved polarizability matching misfits of 0.101, 0.008, which strongly suggests that the target is a 60 mm mortar.

We also present the case of recovering a small caliber UXO (40mm projectile). There are also four survey lines that cover this target of interest. Figures 11-13 show the survey map and the inverted source locations, the recovered polarizabilties, and the observed and predicted responses.

Similar to the second example, the IMLI and the JETSP offer a more accurate recovery of the polarizabilities than the standard method.

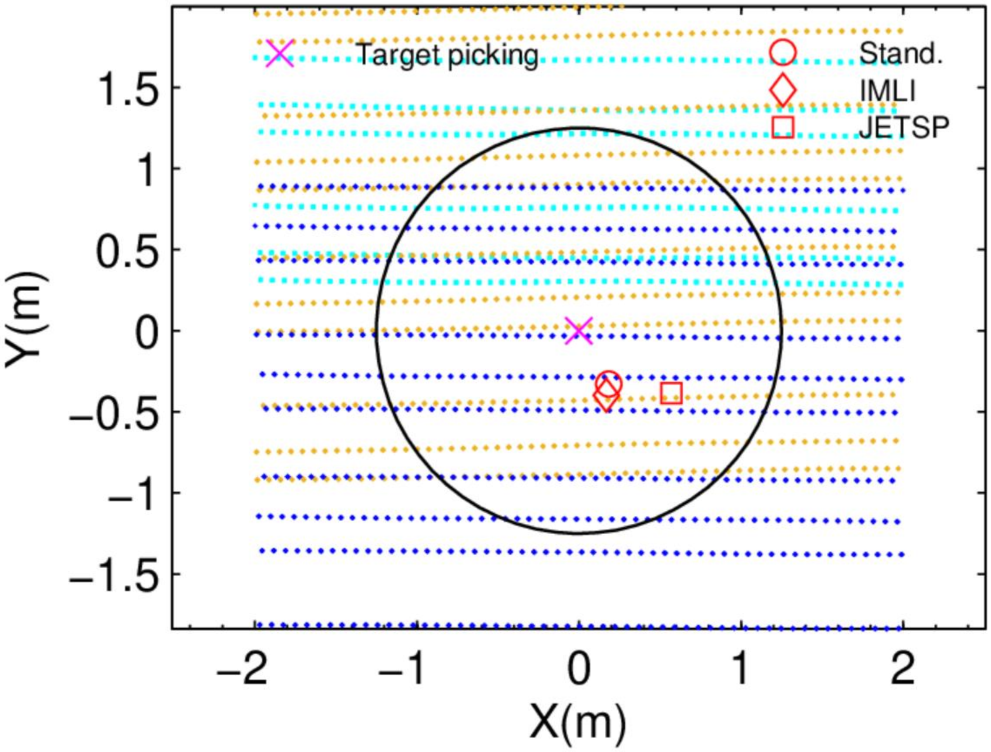

**Figure 5**. Calibration data Example 1. The map of three survey passes, target picking, and the inverted source locations of the three methods. A pass is represented by colored dotted lines, each which denotes the track of one of the receiver cubes.

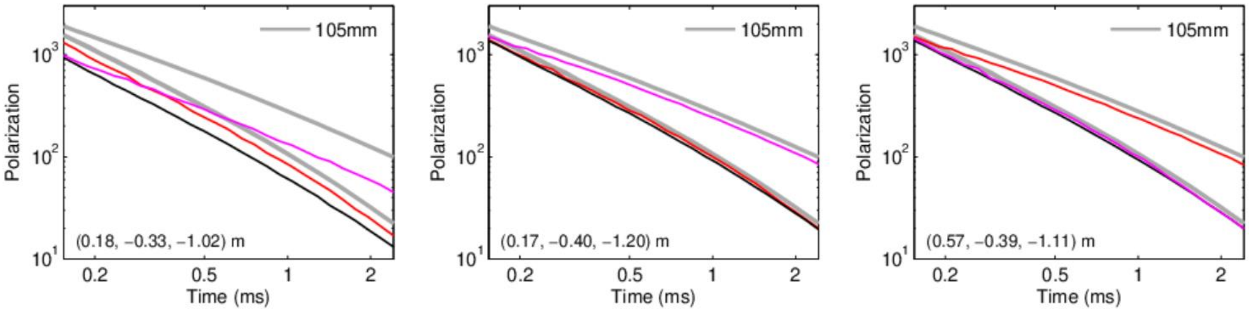

(a) (b) (c)

**Figure 6.** Calibration data Example 1. Recovered polarizabilities from the three inversion methods against the references of 105mm: (a) Standard inversion; (b) IMLI; (c) JETSP. The inverted source location is displayed in each subplot.

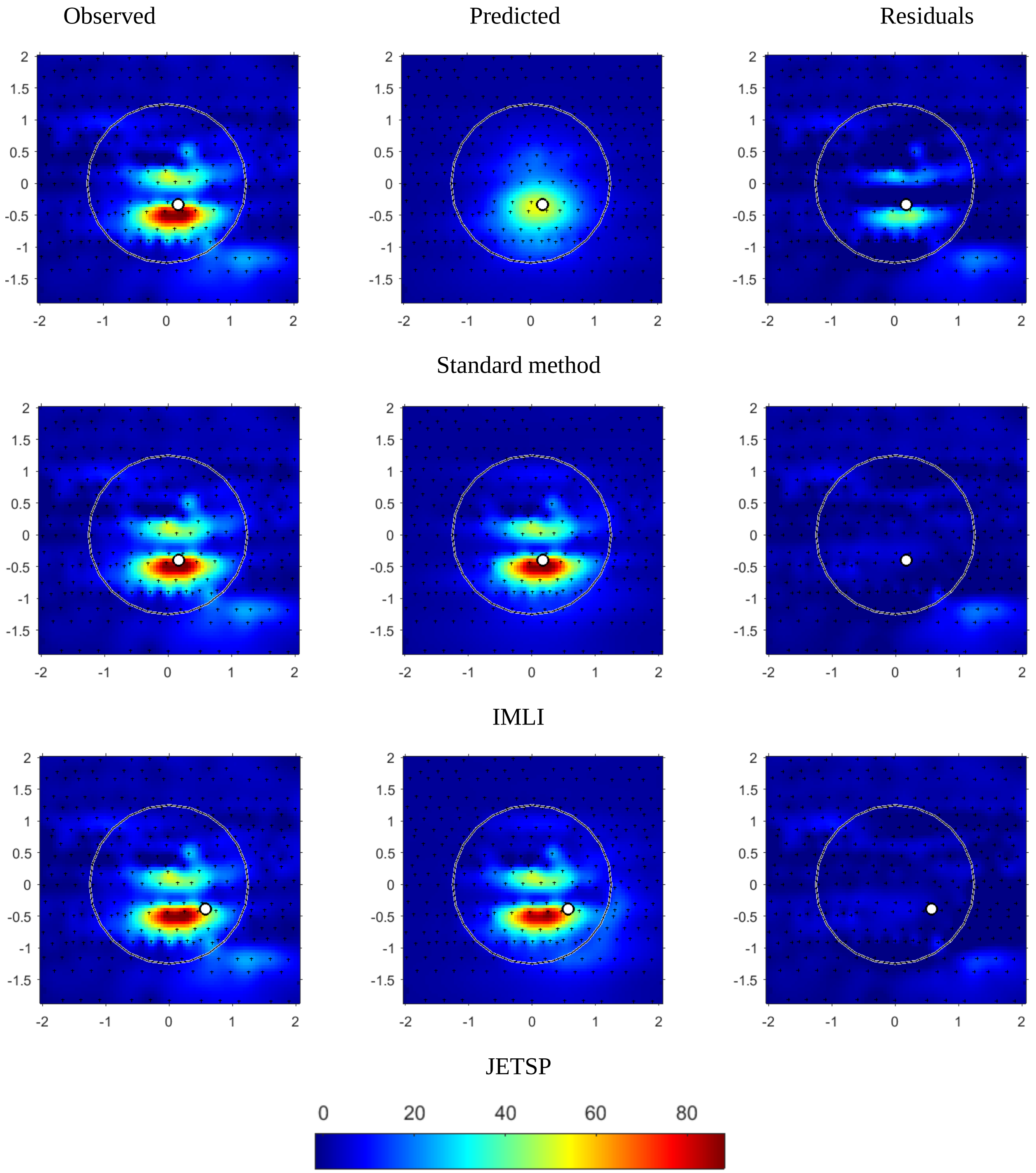

**Figure 7.** Calibration data Example 1. The image of the observed, predicted responses and residuals. Top row: Standard inversion; Middle: IMLI; Bottom: JETSP.

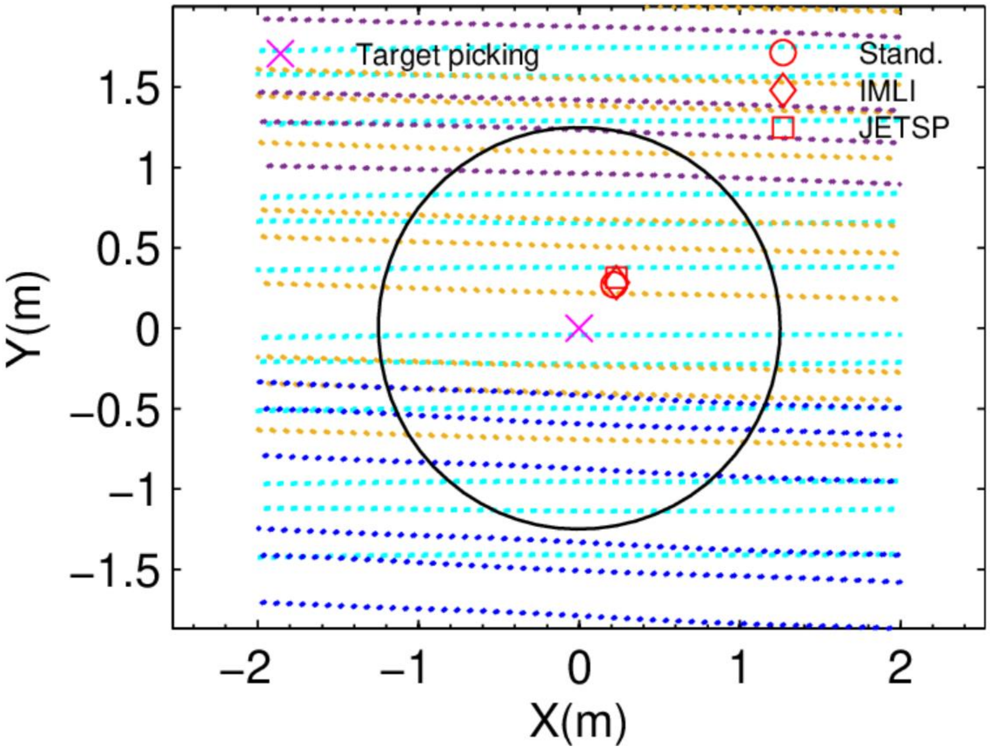

**Figure 8.** Calibration data Example 2. The map of four survey passes, target picking, and the inverted source locations of the three methods. A pass is represented by colored dotted lines, each which denotes the track of one of the receiver cubes.

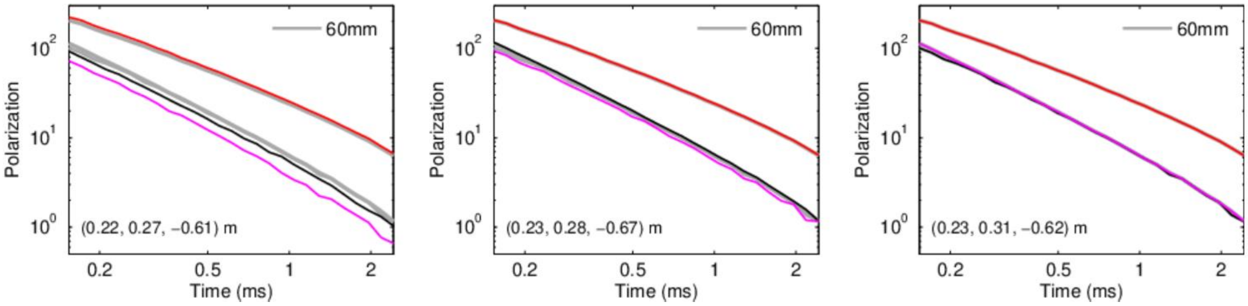

(a) (b) (c)

**Figure 9.** Calibration data Example 2. Recovered polarizabilities from the three inversion methods against the references of 60mm: (a) Standard inversion; (b) IMLI; (c) JETSP. The inverted source location is displayed in each subplot.

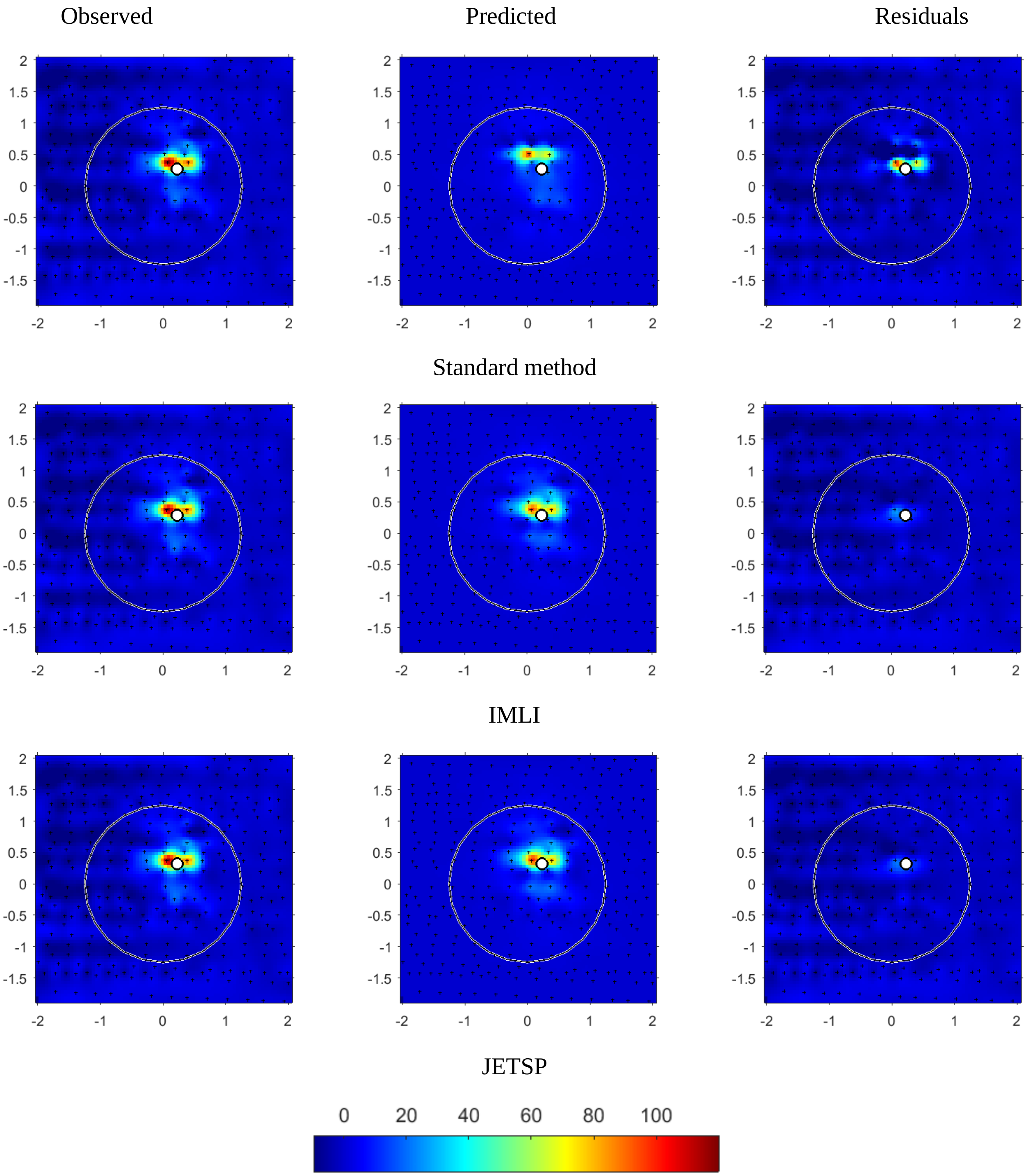

**Figure 10.** Calibration data Example 2. The image of the observed, predicted responses and residuals. Top row: Standard inversion; Middle: IMLI; Bottom: JETSP.

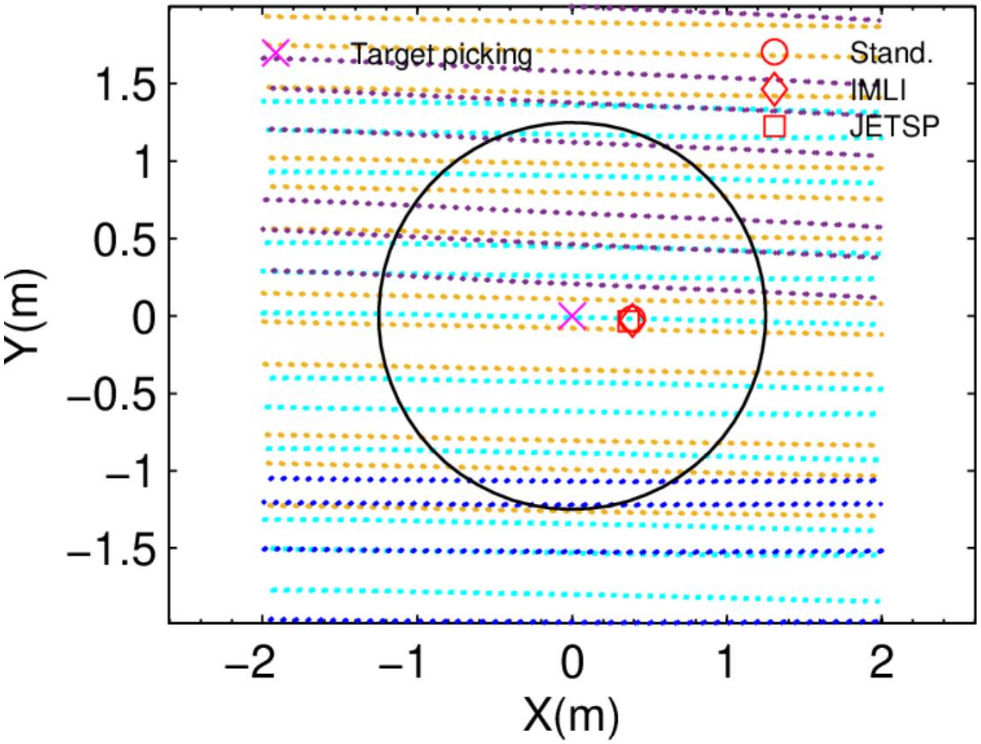

**Figure 11.** Calibration data example 3. The map of four survey passes, target picking, and the inverted source locations of the three methods. A pass is represented by colored dotted lines, each which denotes the track of one of the receiver cubes.

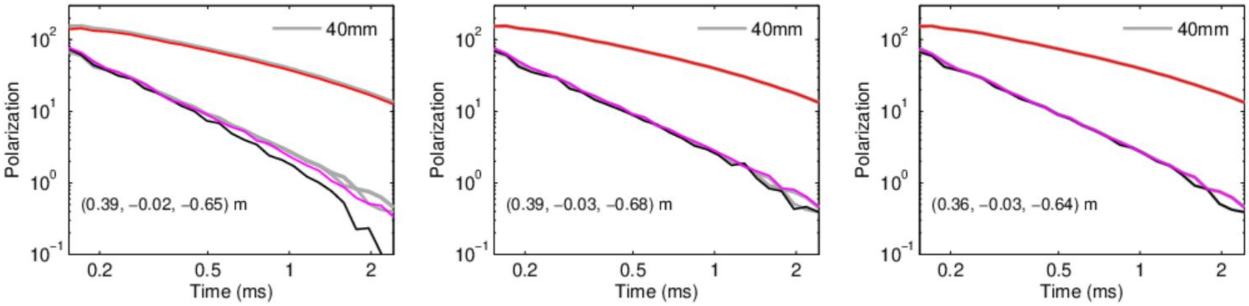

(a) (b) (c)

**Figure 12.** Calibration data example 3. Recovered polarizabilities from the three inversion methods against the references of 40mm: (a) Standard inversion; (b) IMLI; (c) JETSP. The inverted source location is displayed in each subplot.

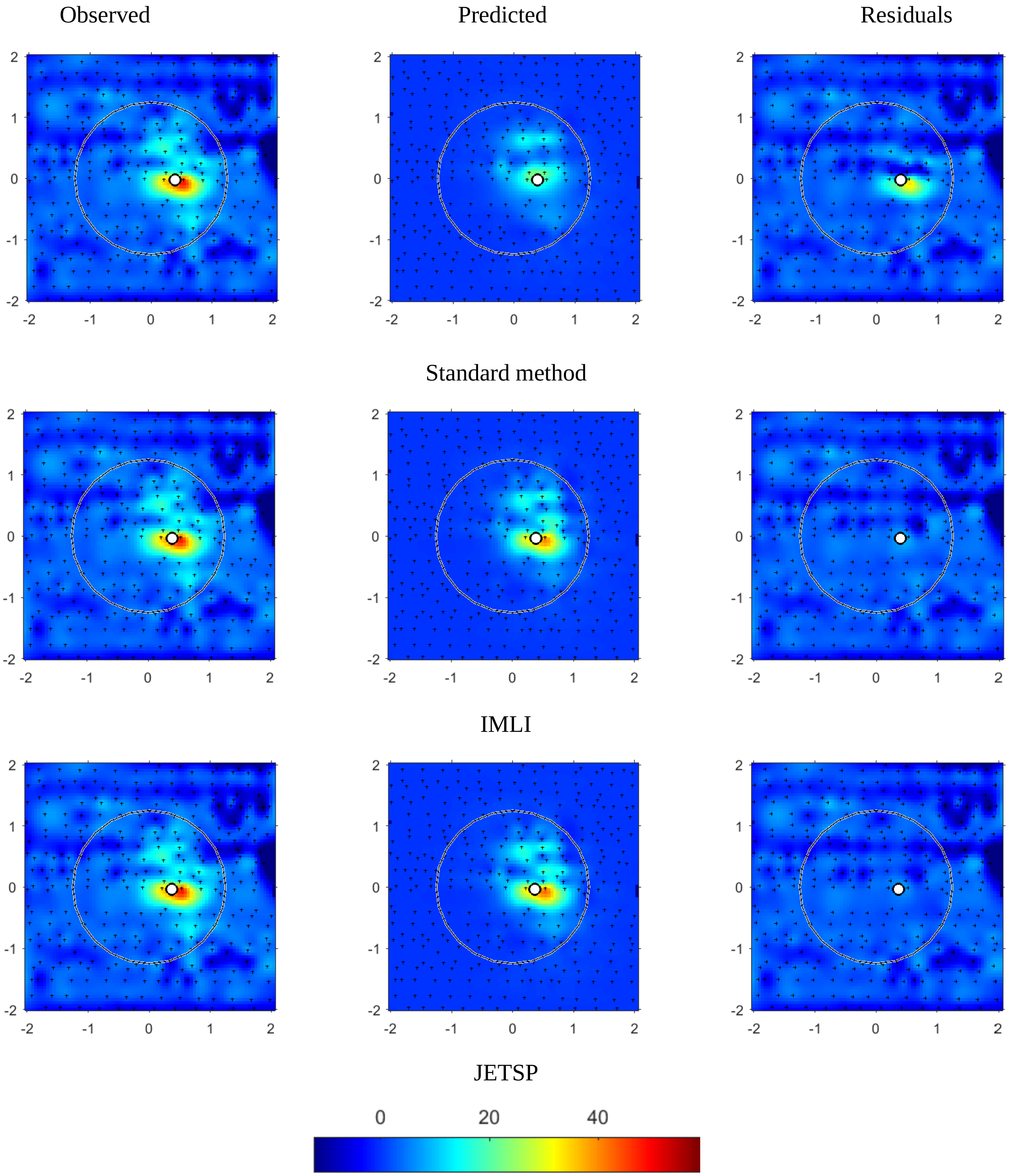

**Figure 13.** Calibration data example 3. The image of the observed, predicted responses and residuals. Top row: Standard inversion; Middle: IMLI; Bottom: JETSP.

### *Blind-grid data examples*

For the Blind Grid, we present an example of recovering the polarizabilities from a 155mm projectile within the 2021 UltraTEMA data (item U001 in the PNNL ground-truth). In this example, only two survey lines (the dotted cyan and orange lines) cover the area of interest in Figure 14. The two passes shown in the section do not overlap. Following the same procedures we used for processing the calibration data, the data within the big circle are inverted using the three methods. The inverted source locations, shown in Figure 14, are given at (-0.29, 0.06, -0.85) m with the standard method, (-0.31, 0.06, -0.94) m with the IMLI, and (-0.22, 0.05, -0.90) m with the JETSP method. The major difference between the IMLI and the JETSP source locations appears in the x-coordinate, which is 9 cm. The three methods seem to model the pattern of the observed response well and have similar magnitude residuals (Figure 16). The polarizabilities recovered by the standard method deviates from the reference with a matching misfit of 0.468, while the polarizabilites recovered by both IMLI and JETSP methods agree well with the ground-truth reference (U001: 155mm projectile) with polarizability matching misfit of 0.225, 0.154, respectively (Figure 15).

In the last example, we present the case of recovering a likely UXO of 81mm extracted from the marine blind data collected in 2022. As shown in Figure 17, there are the two survey lines (the dotted cyan and orange lines) that cover the area of interest. Roughly, half the portion of the circled area is covered by the two lines. Again, the masked data within the black circle are inverted using the three methods. Initially, a single-object inversion is executed with the IMLI method. However, the inversion yields a significant anomaly pattern in the residual map, as illustrated at the top row of Figure 18. This suggests that this may be a multi- object scenario within the field view of the sensing. We opted to process this dataset with two-object models with each of the three methods.

To accompany Figure 18, we show a profile (Figure 19) of the observed and predicted responses, and the residuals at t1 = 0.154 ms for receiver coil 9 (denoted as a solid cyan line in Figure 17). With the two-object inversions, the IMLI produces an improved data fit with significantly reduced residuals. The JETSP method with the two-object inversion has a similar data fitting performance to the IMLI. The standard method with the two-object inversion still has difficulty modelling the observed responses and the associated residuals remain large. The first set of inverted source locations, shown in Figure 17, are given at (-0.69, 0.23, -0.80) m with the standard method, (-0.74, 0.23, -0.85) m with the IMLI, and (-0.78, 0.23, -0.69) m with the JETSP method. The second set of inverted source locations are given in the method order at (-0.02, 0.15, -0.65) m, (-0.05, 0.17, -0.69) m, and (0.20, 0.06, -0.70). It looks that the predicted second IMLI and JETSP source locations exhibit different shifts relative to the picking location, the first to the North the second to the East. Perhaps the most striking point of difference between the standard method and the other two methods can be observed with the two sets of the recovered polarizabilities shown in Figure 20. While the first set of polarizabilities recovered by the standard method may predict a target of interest (larger than 81 mm), although with unequal minor polarizabilites, the second set of recovered polarizabilities likely indicate a non-UXO, with the matching misfit of 0.864 against the 81 mm reference item. On the other hand, the IMLI and the JETSP predict that the two sources have almost identical recovered polarizabilities that match well with the 81 mm reference item. Matching misfits are 0.137 (IMLI-1), 0.222 (JETSP-1), 0.234 (IMLI-2), and 0.057 (JETSP-2).

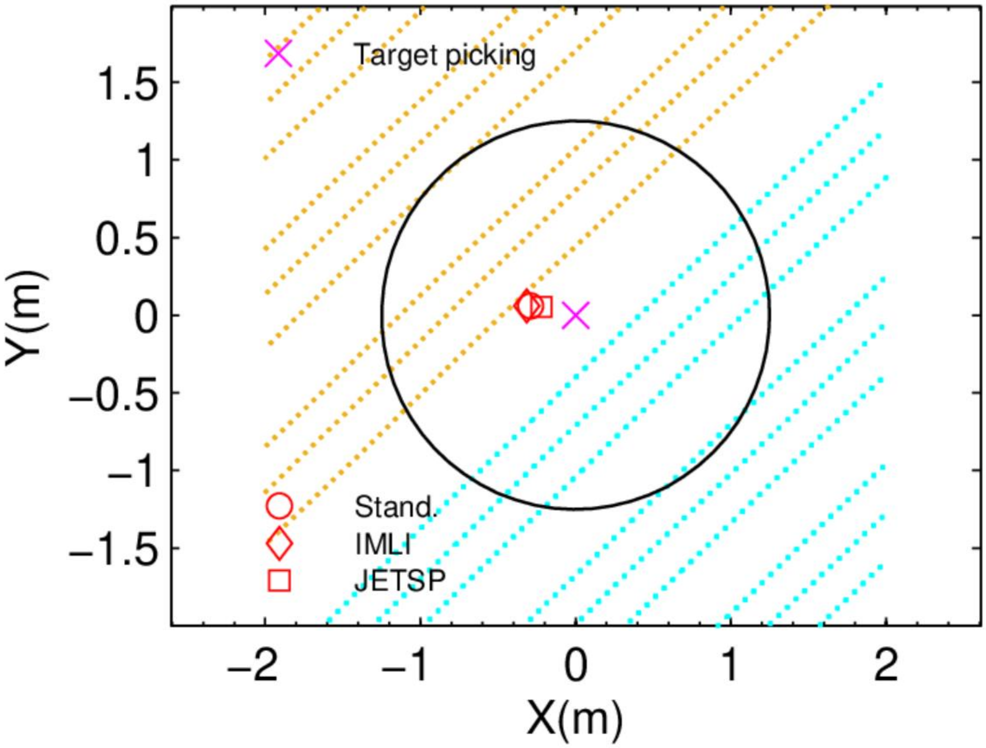

**Figure 14.** Blind-grid data example 1: The map of two survey passes, target picking, and the inverted source locations of the three methods. A pass is represented by colored dotted lines, each which denotes the track of one of the receiver cubes.

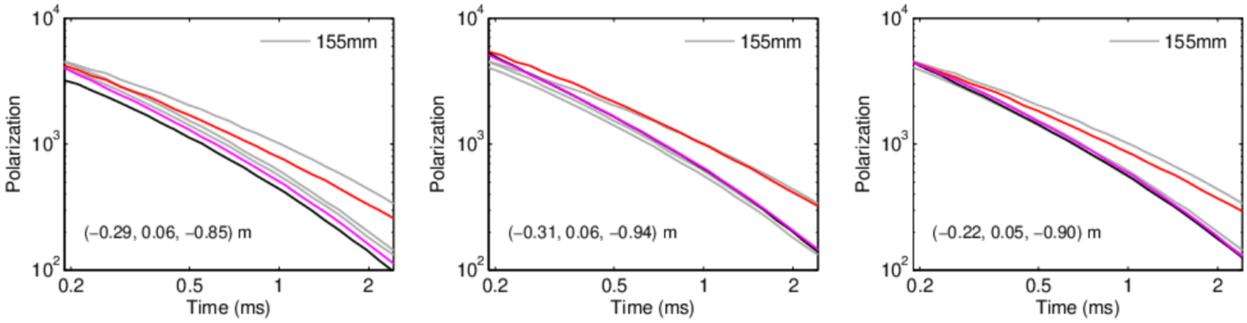

(a) (b) (c)

**Figure 15.** Blind-grid data example 1. Recovered polarizabilities from the three inversion methods against the references of 155mm: (a) Standard inversion; (b) IMLI; (c) JETSP. The inverted source location is displayed in each subplot.

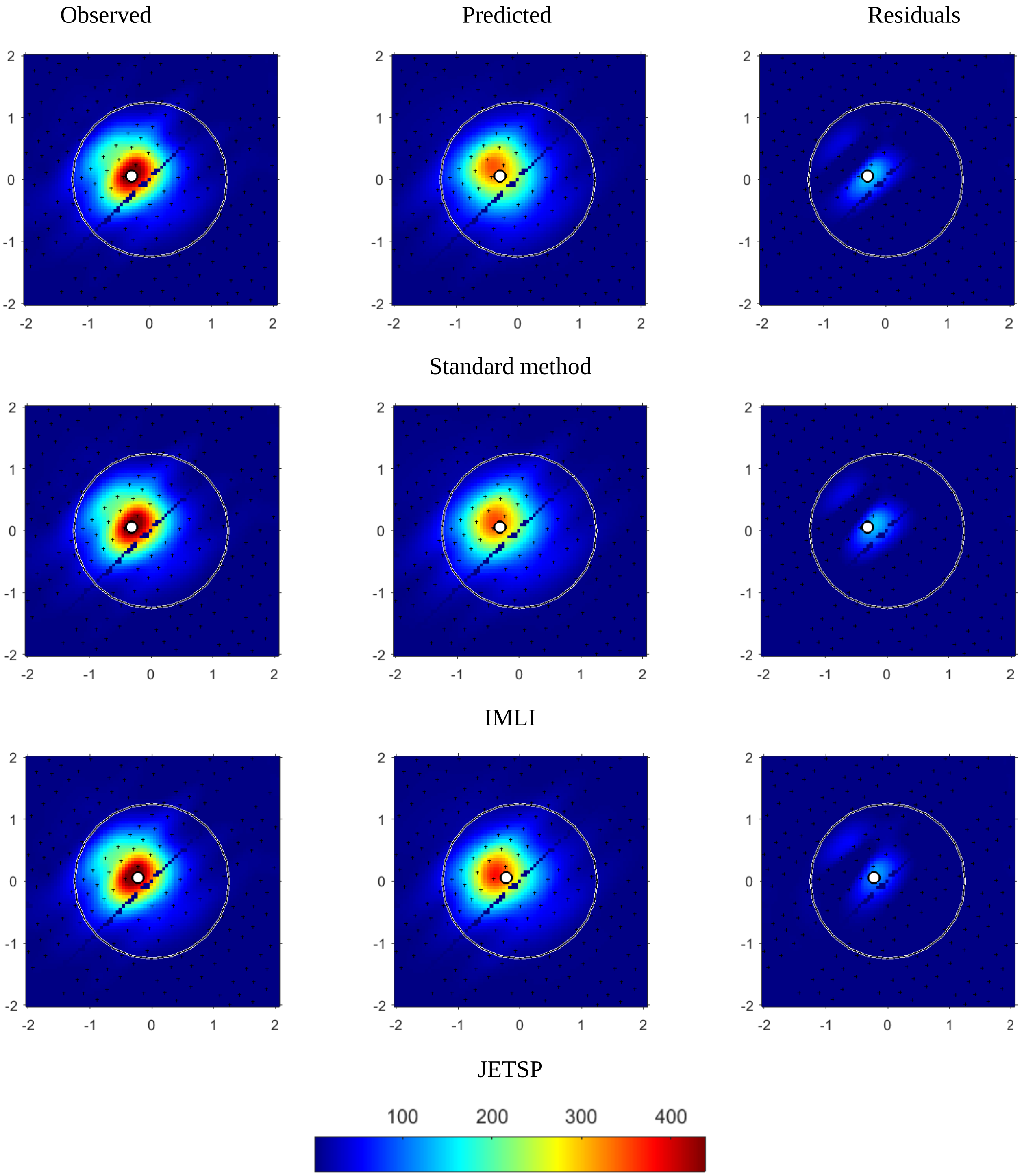

**Figure 16.** Blind-grid data example 1. The image of the observed, predicted responses and residuals. Top row: Standard inversion; Middle: IMLI; Bottom: JETSP.

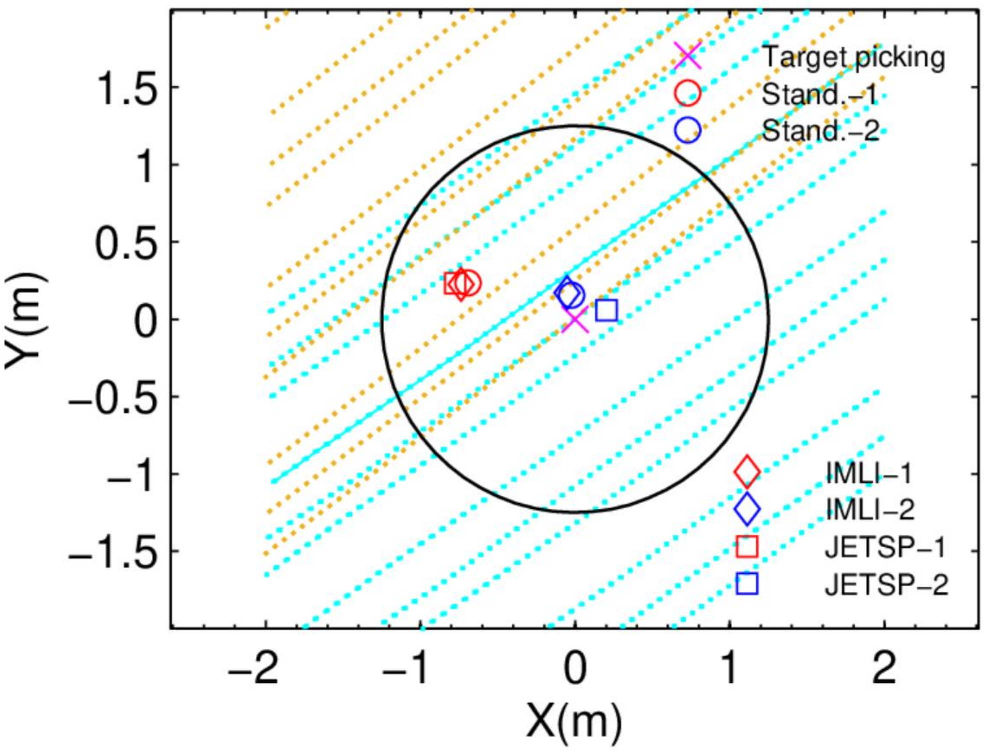

**Figure 17.** Blind-grid data example 2: The map of two survey passes, target picking, and the inverted 2-source locations of the three methods. A pass is represented by colored dotted lines, each which denotes the track of one of the receiver cubes.

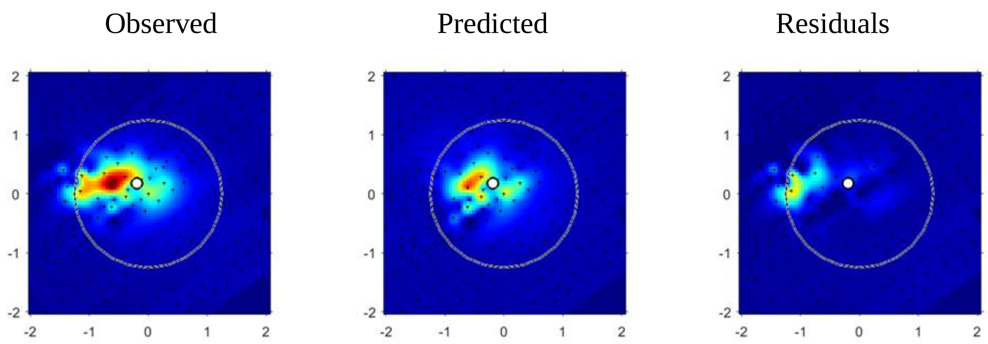

IMLI: single-object inversion

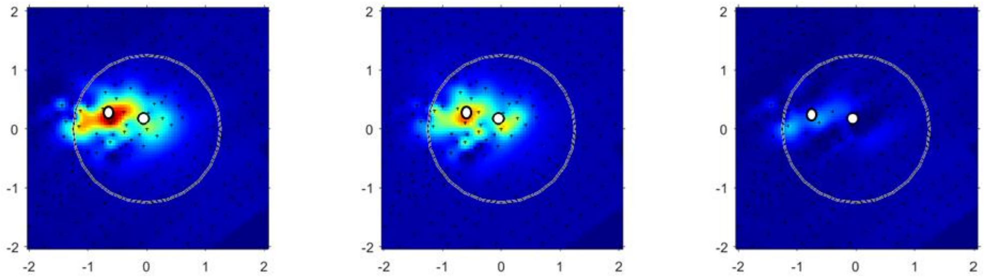

IMLI: 2-object inversion

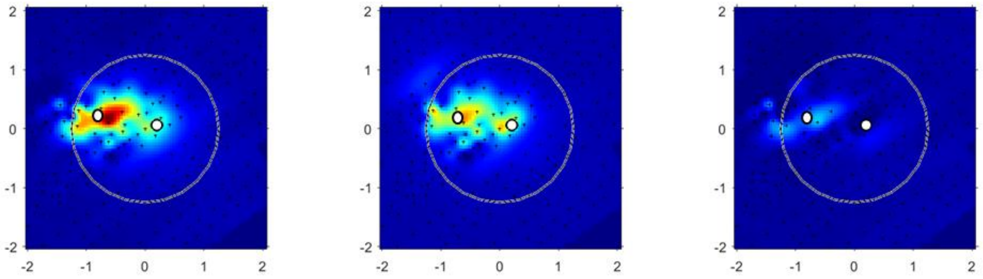

JETSP: 2-object inversion

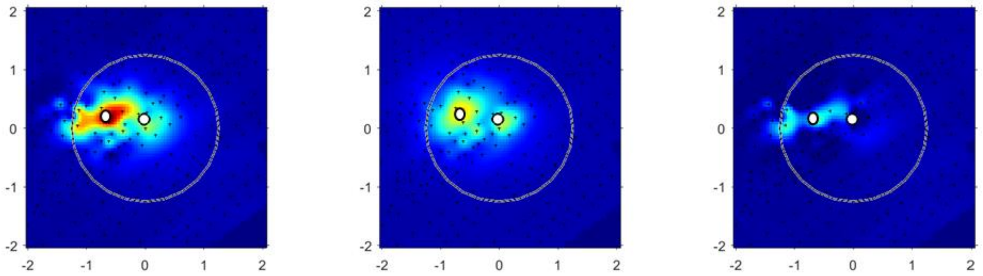

Standard inversion: 2-object inversion

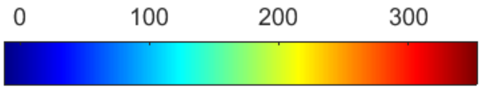

**Figure 18.** Blind-grid data example 2. The image of the observed, predicted responses and residuals. From Top to bottom: Single-object inversion- IMLI; 2-object inversion (2OI)-IMLI; 2OI-JETSP; 2OI-Standard inversion.

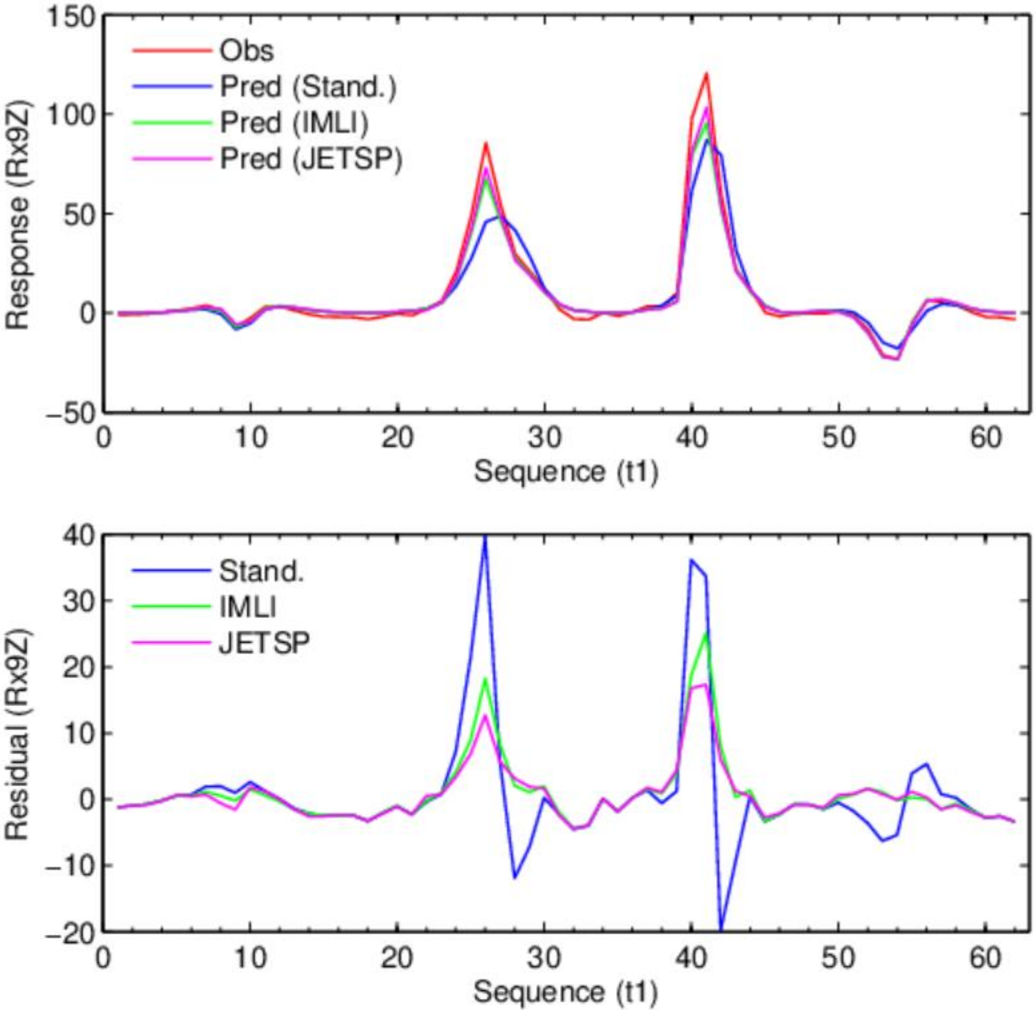

**Figure 19.** Blind-grid data example 2. The profile of the observed, predicted responses, and the residuals at t1 = 0.154 ms for receiver coil 9 (a solid cyan line in Figure 17).

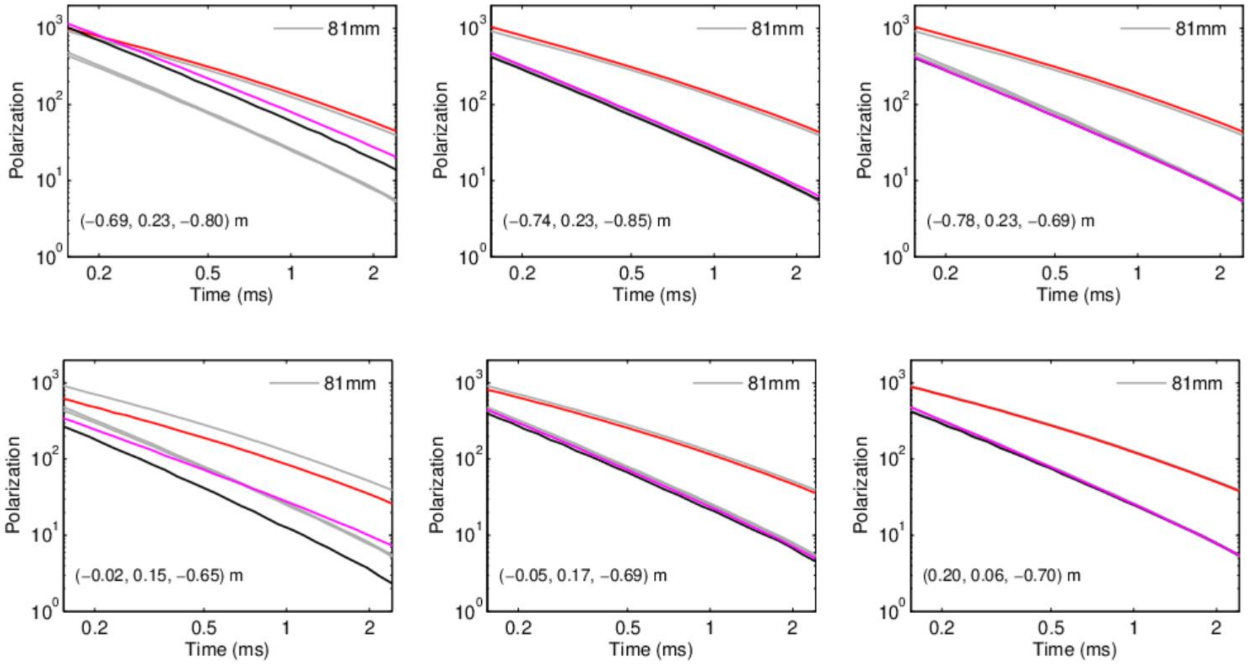

(a) (b) (c)

**Figure 20.** Blind-grid data example 2. Recovered polarizabilities of 2-object inversion (a) Standard inversion. (b) IMLI. (c) JETSP.

# 5. Conclusion

We have presented the two methods, the IMLI and the JETSP algorithms, that are the important extensions to the standard inversion method. Both the IMLI and the JESP are formulated from different perspectives to address the issue of sensor positioning errors. The IMLI algorithm allows sensors from *N* sensing positions to view the targets as *N* sets of virtual sources that have intermediate and independent locations but with invariant physical properties. We say that the IMLI is designed to implicitly take into account the sensor positioning errors. In the JETSP algorithm, sensing location perturbations $\Delta\mathbf{s}_n$ are directly introduced as unknowns that are additional to extrinsic target parameters $(\mathbf{r},\ \boldsymbol{\theta})$. The JETSP formulation can be seen as a processing perspective reversed from the IMLI in that targets are presented to “view” at those sensing deployments that need to be adjusted from nominal positions for being consistent with the observed responses and the actual geometrical presence $(\mathbf{r},\ \boldsymbol{\theta})$ of targets as well. The examples presented here show that the two extended methods help overcome the impacts of sensor positional uncertainty on the inversion and thus are able to accurately recover the polarizabilites of a target.

In the IMLI the final set of extrinsic source parameters are estimated under uncertain sensor positions and may turn out to be inaccurate. We are experimenting with different methods to deal with this potential location trade-off and inaccuracy. Similarly, in the JETSP formulation as we jointly solve for both source and sensing parameters, the algorithm can introduce a solution trade-off between the two sets of parameters that may cause bias in the target locations. This potential trade-off problem warrants further investigation.

# 6. References

1. Len Pasion and Lin-Ping Song, SERDP MR-2318: Strategies and methods for Effective UXO Classification, 2021.

2. Internal Validation of Independent Model Location Inversion (IMLI), BTG, 2022.

3. L.-P. Song, L. R. Pasion, S. D. Billings, and D. W. Oldenburg, “Nonlinear inversion for multiple objects in transient electromagnetic induction sensing of unexploded ordnance: technique and applications,” IEEE Transactions on Geoscience and Remote Sensing, vol. 49, no. 10, pp. 4007–4020, 2011.

4. S. D. Billings, R. Funk, J. Gamey, ESTCP MR19-5073: UltraTEM Marine towed system for detection and characterization of buried ordnance, 2021.